Clim. Past, 12, 339–375, 2016
www.clim-past.net/12/339/2016/
doi:10.5194/cp-12-339-2016

Climate of the Past
Open Access
EGU

Effects of eustatic sea-level change, ocean dynamics, and nutrient utilization on atmospheric pCO_2 and seawater composition over the last 130 000 years: a model study

K. Wallmann[1], **B. Schneider**[2], **and M. Sarnthein**[2,3]

[1]GEOMAR Helmholtz Centre for Ocean Research Kiel, Wischhofstr. 1–3, 24148 Kiel, Germany
[2]Institut für Geowissenschaften, University of Kiel, Olshausenstr. 40, 24098 Kiel, Germany
[3]Institut für Geologie, University of Innsbruck, Innrain 50, 6020 Innsbruck, Austria

Correspondence to: K. Wallmann (kwallmann@geomar.de)

Received: 19 May 2015 – Published in Clim. Past Discuss.: 29 June 2015
Revised: 15 January 2016 – Accepted: 20 January 2016 – Published: 18 February 2016

Abstract. We have developed and employed an Earth system model to explore the forcings of atmospheric pCO_2 change and the chemical and isotopic evolution of seawater over the last glacial cycle. Concentrations of dissolved phosphorus (DP), reactive nitrogen, molecular oxygen, dissolved inorganic carbon (DIC), total alkalinity (TA), ^{13}C-DIC, and ^{14}C-DIC were calculated for 24 ocean boxes. The bi-directional water fluxes between these model boxes were derived from a 3-D circulation field of the modern ocean (Opa 8.2, NEMO) and tuned such that tracer distributions calculated by the box model were consistent with observational data from the modern ocean. To model the last 130 kyr, we employed records of past changes in sea-level, ocean circulation, and dust deposition. According to the model, about half of the glacial pCO_2 drawdown may be attributed to marine regressions. The glacial sea-level low-stands implied steepened ocean margins, a reduced burial of particulate organic carbon, phosphorus, and neritic carbonate at the margin seafloor, a decline in benthic denitrification, and enhanced weathering of emerged shelf sediments. In turn, low-stands led to a distinct rise in the standing stocks of DIC, TA, and nutrients in the global ocean, promoted the glacial sequestration of atmospheric CO_2 in the ocean, and added ^{13}C- and ^{14}C-depleted DIC to the ocean as recorded in benthic foraminifera signals. The other half of the glacial drop in pCO_2 was linked to inferred shoaling of Atlantic meridional overturning circulation and more efficient utilization of nutrients in the Southern Ocean. The diminished ventilation of deep water in the glacial Atlantic and Southern Ocean led to significant ^{14}C depletions with respect to the atmosphere. According to our model, the deglacial rapid and stepwise rise in atmospheric pCO_2 was induced by upwelling both in the Southern Ocean and subarctic North Pacific and promoted by a drop in nutrient utilization in the Southern Ocean. The deglacial sea-level rise led to a gradual decline in nutrient, DIC, and TA stocks, a slow change due to the large size and extended residence times of dissolved chemical species in the ocean. Thus, the rapid deglacial rise in pCO_2 can be explained by fast changes in ocean dynamics and nutrient utilization whereas the gradual pCO_2 rise over the Holocene may be linked to the slow drop in nutrient and TA stocks that continued to promote an ongoing CO_2 transfer from the ocean into the atmosphere.

1 Introduction

The discussion of mechanisms that might be responsible for the glacial to interglacial change in the atmosphere's CO_2 content is focused on the ocean (Broecker, 1982b). Ever-increasing evidence suggests that CO_2 sequestered in the glacial ocean was rapidly released into the atmosphere at glacial terminations (Schmitt et al., 2012). The fast decline in dust-bound iron deposition in the Southern Ocean (Martin, 1990; Martınez-Garcia et al., 2014) and upwelling pulses in the Southern Ocean (Anderson et al., 2009) and North Pacific (Rae et al., 2014) may have induced the stepwise pCO_2 rise documented in the deglacial ice-core record (Marcott et al., 2014). The preceding CO_2 uptake in the glacial ocean may be attributed to enhanced export production, elevated

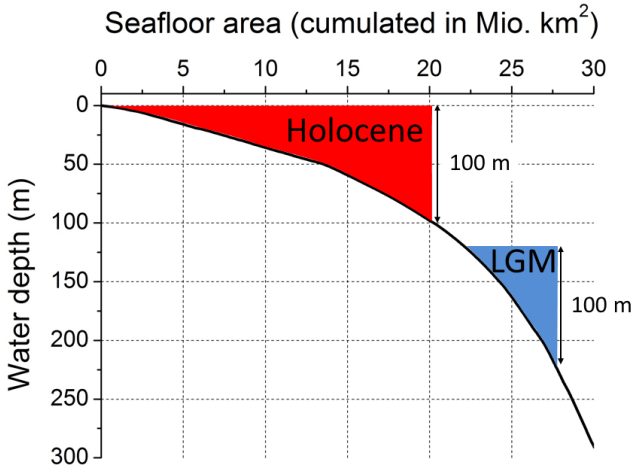

Figure 1. Morphology of global ocean margin. The black line is the cumulated seafloor area as derived from the high-resolution ETOPO 1 grid (Eakins and Sharman, 2012). The ocean margin at 0–100 m water depth is indicated for the modern ocean (red area) and for the LGM when eustatic sea-level was lowered by 120 m (blue area). The global ocean retreated into steeper terrain during the glacial marine regression. The seafloor areas covered by shallow waters were reduced by this steepening of ocean margins.

seawater alkalinity, and changes in ocean dynamics. The biological pump was probably intensified by iron fertilization (Martin, 1990) and the coeval expansion of nitrate (Deutsch et al., 2004) and phosphate (Broecker, 1982b) stocks in the glacial ocean, while seawater alkalinity may have been enhanced by the demise of neritic carbonate formation (Berger, 1982; Opdyke and Walker, 1992; Kleypas, 1997). The sequestration of atmospheric pCO_2 in the glacial ocean may have been further promoted by the glacial shoaling of the Meridional Overturning Circulation (MOC) in the Atlantic (Duplessy et al., 1988; Sarnthein et al., 1994), a possible increase in Southern Ocean stratification (Toggweiler, 1999), a prolonged residence time of surface waters in the Southern Ocean providing more time for the biota to draw down nutrients and CO_2 (Watson et al., 2015) and a global decline in MOC intensity and deep ocean ventilation (Sarnthein et al., 2013).

In part, a glacial rise in nitrate, phosphate, and alkalinity concentrations, which may have contributed significantly to the drawdown of atmospheric pCO_2, can be explained by eustatic sea-level fall (Wallmann, 2014). It led to a retreat of ocean margins to steeper terrains that reduced the seafloor area located in shallow waters (Fig. 1). The standing stocks of carbon and nutrients in the glacial ocean may have been significantly enhanced by the marine regression and the decrease in shallow margin area since major removal fluxes – namely accumulation of neritic carbonate, benthic denitrification, burial of particulate organic carbon (POC) and phosphorus (P) – depend on the extent of seafloor located in shallow waters. Various authors and Earth system models considered the glacial decrease in shelf carbonate burial as a major driver of ocean chemistry and atmospheric pCO_2 change (Berger, 1982; Opdyke and Walker, 1992; Brovkin et al., 2012; Ganopolski et al., 1998), since neritic carbonates contribute $\geq 50\,\%$ to the carbonate accumulation at the global seafloor (Milliman and Droxler, 1996; Kleypas, 1997; Berelson et al., 2007). However, the effects of sea-level change on POC and nutrient cycling are largely ignored in these state-of-the-art models even though $> 50\,\%$ of the global benthic denitrification and burial of marine POC and P occur in shelf and upper slope environments (Berner, 1982; Bohlen et al., 2012; Wallmann, 2010).

Against this background, our contribution aims to explore and quantify the effects of sea-level change, ocean dynamics, and nutrient utilization on seawater composition and atmospheric pCO_2 over the last glacial cycle. We use a simple Earth system box model to simulate both chemical and isotopic changes in seawater composition and employ isotope data ($\delta^{13}C$) to constrain changes in ocean dynamics and deep ocean ventilation. Atmospheric pCO_2 and the distributions of dissolved oxygen, carbonate, and radiocarbon in the glacial ocean serve as key prognostic model variables. They are compared with independent proxy data to address the following specific questions: What fraction of the glacial pCO_2 drawdown can be ascribed to eustatic sea-level fall (Wallmann, 2014)? To which degree do global ^{14}C data sets assembled by Sarnthein et al. (2013, 2015) actually reflect our concepts and ideas on glacial and deglacial ocean circulation and carbon cycling? Do marine ^{14}C data really form a quantitative proxy of DIC in the glacial deep ocean as proposed by Sarnthein et al. (2013)? To avoid circular reasoning, dissolved oxygen, carbonate, and radiocarbon distributions calculated for the glacial ocean were not used to parametrize our model. These distribution patterns and the atmospheric pCO_2 values calculated in the model are non-trivial consequences of interactions between the various model components and thus are employed to validate the model performance.

2 Model set-up

The atmospheric partial pressure of CO_2 (pCO_2) serves as the key prognostic variable of the new multi-box Earth system model presented in this paper. It was calculated considering continental weathering and degassing processes and gas exchange with the surface ocean (Wallmann, 2014). The oceans were represented by 24 boxes (Fig. 2). The major ocean basins North Atlantic (NA, 30–60° N), Tropical Atlantic (TA, 30° N–30° S), Southern Ocean (SO, > 30° S), Tropical Indo-Pacific (TIP, 30° N–30° S), North Pacific (NP, 30–60° N), and Arctic Ocean (AR, > 60° N; including the Greenland–Norwegian Sea) each were divided into surface, intermediate, deep, and bottom water boxes extending from 0–100, 100–2000, 2000–4000, to > 4000 m water depth, re-

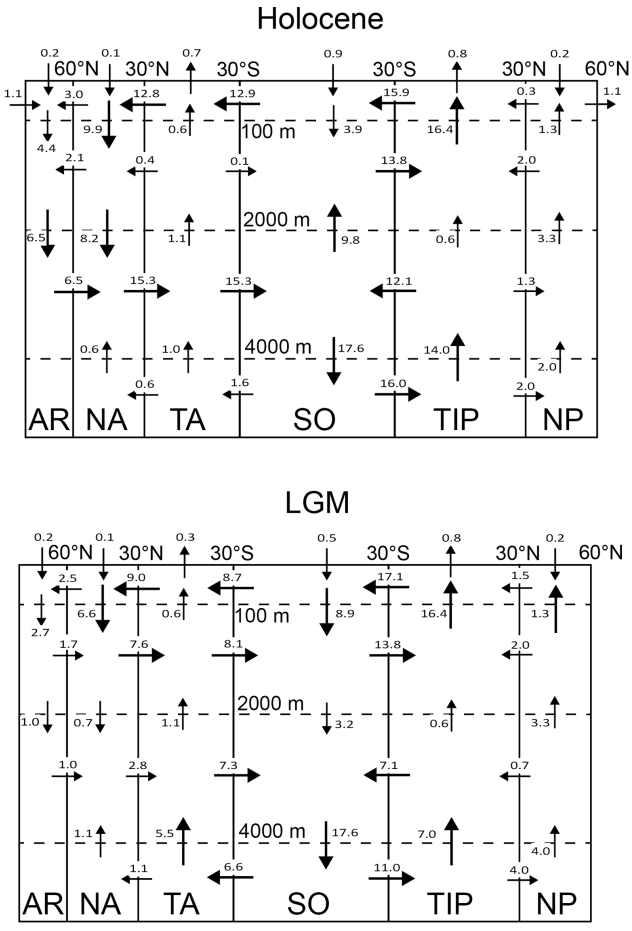

Figure 2. Set-up of the box model: the global ocean is separated into 24 boxes representing surface (0–100 m), intermediate (100–2000 m), deep (2000–4000 m), and bottom (> 4000 m) waters in the Arctic (AR), North Atlantic (NA), Tropical Atlantic (TA), Southern Ocean (SO), Tropical Indo-Pacific (TIP), and North Pacific (NP). Arrows with numbers indicate net water fluxes between boxes in Sv; major fluxes (> 5 Sv) are represented by large arrows, minor fluxes (< 5 Sv) by small arrows. Arrows crossing the top boundary of the surface water boxes (seawater–atmosphere interface) indicate net freshwater fluxes (precipitation + river water fluxes – evaporation). The upper panel shows the circulation field applied for the modern ocean and the previous interglacial; the lower panel shows the circulation applied over the LGM.

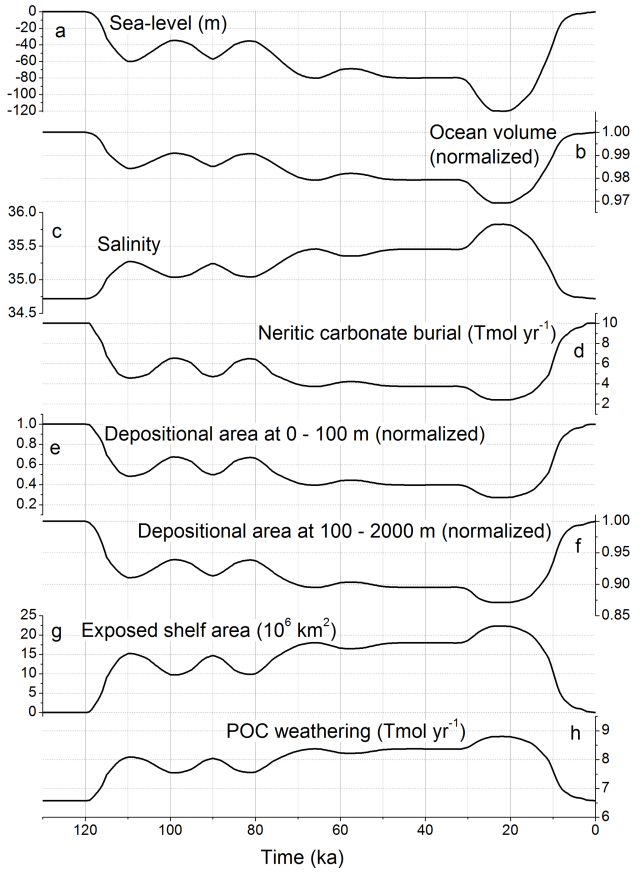

Figure 3. Model forcing related to sea-level change. **(a)** Eustatic sea-level (Waelbroeck et al., 2002; Stanford et al., 2011); **(b)** global ocean volume as calculated from eustatic sea-level and ocean bathymetry data (Eakins and Sharman, 2012); **(c)** salinity of global mean seawater as calculated from global ocean volume; **(d)** global burial rate of neritic carbonate as calculated from seafloor area at 0–50 m water depth (Kleypas, 1997; Wallmann, 2014); **(e–f)** seafloor area at 0–100 m and 100–2000 m water depth calculated from sea-level and ocean bathymetry data (Eakins and Sharman, 2012); **(g)** exposed shelf area calculated from sea-level and ocean bathymetry data (Eakins and Sharman, 2012); **(h)** global rate of POC weathering calculated from exposed shelf area (Wallmann, 2014).

spectively. The following tracer concentrations were calculated as prognostic variables for each of the water boxes: salinity (Sal), dissolved phosphorus (DP), dissolved reactive nitrogen (DN), dissolved oxygen (DO), total alkalinity (TA), dissolved inorganic carbon (DIC), dissolved inorganic ^{13}C (^{13}C-DIC), and dissolved inorganic radiocarbon (^{14}C-DIC). Details of the model set-up are given in Appendix A.

Eustatic sea-level change was applied as major model forcing (Fig. 3). Changes in global ocean volume, salinity, depositional area at continental margins, and exposed shelf area were derived from the sea-level record (Stanford et al., 2011; Waelbroeck et al., 2002) and the hypsographic curve (Eakins and Sharman, 2012). The burial rate of neritic carbonates was reduced during marine regressions in proportion to the decrease in seafloor area available for the growth of tropical reefs and carbonate platforms (Appendix B). We tested the degree to which the decrease in seafloor area at 0–100 and 100–2000 m water depth during glacial sea-level low-stands affected benthic denitrification and the burial of organic carbon and marine phosphorus on the continental shelf and slope (Appendix B) while we assumed that carbonate, P, and POC weathering were promoted by the exposure of shelf sediments (Appendix A).

The comprehensive geological database on benthic foraminiferal δ^{13}C (Oliver et al., 2010; Sarnthein et al., 1994) was employed to constrain water fluxes for the Last Glacial Maximum (LGM). Mean δ^{13}C-DIC values were calculated for those ocean boxes where sufficient δ^{13}C data were available and compared to model results. Water fluxes were varied until the Holocene–LGM differences in δ^{13}C generated by the model were consistent with the differences recorded in foraminifera (Table A5). The tuning was done using full transient runs with all forcings applied. The resulting fluxes are shown in Fig. 2. The southward water flux from the Atlantic into the Southern Ocean was relocated from deep (2000–4000 m) to intermediate waters (100–2000 m) to mimic the shoaling of the Atlantic Meridional Overturning Circulation (AMOC) which is inferred not only from δ^{13}C data but also from various other proxy records (Curry and Oppo, 2005; Piotrowski et al., 2005; Roberts et al., 2010). Bottom water fluxes from the Southern Ocean into the Atlantic were enhanced during the LGM while the northward flow of surface water was reduced. The overall water exchange between the Atlantic and Southern Ocean was maintained constant at 15.4 Sv. The bottom and deep water exchange between the Southern Ocean and the Indo-Pacific was reduced by 5 Sv to reproduce the δ^{13}C data (Table A5).

The eustatic sea-level curve (Fig. 3a) was applied to change ocean dynamics continuously over time so as to define water fluxes over the full model period (Fig. 4a–c). Thus we assumed that AMOC shoaled gradually during the transition from interglacial to full glacial conditions (130–21 ka) while the horizontal exchange flux of intermediate waters between the Southern Ocean and Tropical Indo-Pacific was enhanced over the glacial to mimic the ventilation of tropical oxygen minimum zones (OMZs) observed in various proxy records (Altabet et al., 1995; Jaccard and Galbraith, 2012). Additional rapid changes were implemented for the deglacial period (Fig. 4a and d). NADW formation was strongly reduced during Heinrich Event 1 (H1) and the Younger Dryas (McManus et al., 2004) while upwelling pulses were prescribed in the Southern Ocean during H1 and the Bølling-Allerød (Anderson et al., 2009; Skinner et al., 2010) and in the North Pacific during H1 (Rae et al., 2014). Timing and intensity of these deglacial upwelling/ventilation events were varied until Δ^{14}C-DIC values calculated for deep and surface water boxes were consistent with Δ^{14}C values recorded in benthic and pelagic foraminifera (Fig. A2). In addition, the deglacial ice-core record of pCO_2 (Marcott et al., 2014) and biogenic opal accumulation rates (Anderson et al., 2009) were employed to constrain the timing and intensity of upwelling pulses in the Southern Ocean. The iron accumulation record from site ODP 1090 was used to constrain changes in nutrient utilization in the Southern Ocean (Martınez-Garcia et al., 2014) assuming that the increase in iron accumulation observed at this site directly translates into an increase in the efficiency of nutrient utilization (Fig. 4e). To calculate realistic marine isotope trends, the changing isotopic compositions of atmospheric CO_2 were set to the values documented in the geological record (Fig. 4f–g). Atmospheric δ^{13}C-CO_2 was not calculated as a prognostic model variable because a biased vertical δ^{13}C-DIC gradient in the Southern Ocean impeded the simulation of ^{13}C-CO_2 fluxes across the ocean/atmosphere interface (Appendix A, Sect. A8, Fig. A3).

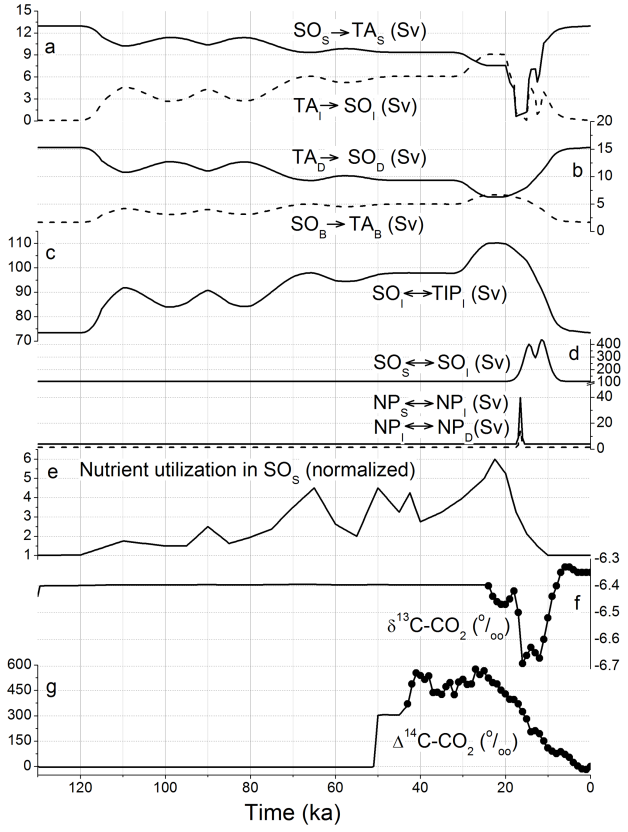

Figure 4. Model forcing applied to define ocean circulation, nutrient utilization in the Southern Ocean, and the isotopic composition of atmospheric CO_2. **(a–b)** Net water fluxes between the Southern Ocean (SO) and Tropical Atlantic (TA). The horizontal flows are given for (from top to bottom) surface water (subscript S), intermediate water (subscript I), deep water (subscript D), and bottom water (subscript B); **(c)** horizontal exchange flux between the Southern Ocean and Tropical Indo-Pacific intermediate waters; **(d)** vertical water exchange fluxes in the Southern Ocean and North Pacific across 100 m water depth (solid lines) and 2000 m water depth (broken line); **(e)** nutrient utilization in the Southern Ocean (Martınez-Garcia et al., 2014); **(f)** δ^{13}C value of atmospheric CO_2. Dots indicate ice-core data (Schmitt et al., 2012) while the solid line defines the values applied in the model. For > 24 kyr BP, where data are not available, the δ^{13}C-CO_2 value is set to −6.4 ‰; **(g)** Δ^{14}C value of atmospheric CO_2, dots indicate values reconstructed from the geological record (Reimer et al., 2013) while the solid line defines the values applied in the model. For > 50 kyr BP, where data are not available, the atmospheric Δ^{14}C-CO_2 is assumed to correspond to the pre-anthropogenic modern value (0 ‰).

The major limitations of our simple box model are (i) very low spatial resolution, (ii) water fluxes between model boxes that are not derived from internal model dynamics, (iii) terrestrial inventories of POC in vegetation and soil that are kept constant over the model period.

As a consequence of low resolution, OMZs are not resolved by our model since the entire Indo-Pacific intermediate water at 100–2000 m water depth is pooled in a single ocean box. In our model, we prescribe a constant rate of pelagic denitrification since we are not able to resolve OMZs. Rates of benthic denitrification and P burial are only moderately affected by the lack of OMZs since the area where OMZs impinge the seafloor only amounts to 1 % of the global seafloor (Bohlen et al., 2012).

The modern water fluxes applied to our box model are based on a dynamically consistent circulation field. As explained in Appendix A, these fluxes were modified to obtain tracer distributions that are consistent with observations in the pre-industrial modern ocean (Fig. A1). Glacial and deglacial changes in ocean circulation were not derived from ocean models but from $\delta^{13}C$ records (Table A5) and additional geochemical observations (Fig. A2). Models with explicit ocean dynamics are superior to any kind of physically unconstrained box model if they generate results that are consistent with observations. However, the physically constrained Earth system models that we are aware of are not yet able to reproduce as many tracer and proxy data as our box model. Our paper shows that shelf and sea-level effects help to explain a wide range of findings (Sect. 3) and we think that the outputs of physically better-constrained models may improve in the case these effects are included in the model architecture. It is not our intention to promote box modelling per se as the method of choice. Rather, we hope that the concepts and ideas advanced in our paper may stimulate the community and help to further enhance cutting-edge Earth system models with explicit ocean dynamics (Tschumi et al., 2011; Menviel et al., 2012; Brovkin et al., 2012; Roth et al., 2014; Lambert et al., 2015).

For many decades it was widely assumed that the modern terrestrial carbon pool exceeds the glacial pool by hundreds of Gt because of biosphere regrowth after the glacial termination (Köhler and Fischer, 2004). This concept was initially developed to explain reduced $\delta^{13}C$ values in glacial seawater (Shackleton, 1977). However, the latest assessment of terrestrial carbon pools indicates that the sum of the modern stocks does not exceed the LGM stock (Brovkin and Ganopolski, 2015). Moreover, this new view on terrestrial carbon cycling suggests a deglacial decline in total carbon stocks since the carbon release from high-latitude areas (melting permafrost soils and soils exposed by the retreat of glacial ice sheets) exceeded the carbon uptake by biosphere regrowth and peat accumulation. Our model explains deglacial and Holocene pCO_2 dynamics and the low glacial $\delta^{13}C$ values by marine processes and sea-level change only. However, we acknowledge that terrestrial processes that are neglected in our model may have played a role especially over the Holocene even though more work needs to be done to constrain the sign and magnitude of terrestrial effects on $\delta^{13}C$ and pCO_2 dynamics.

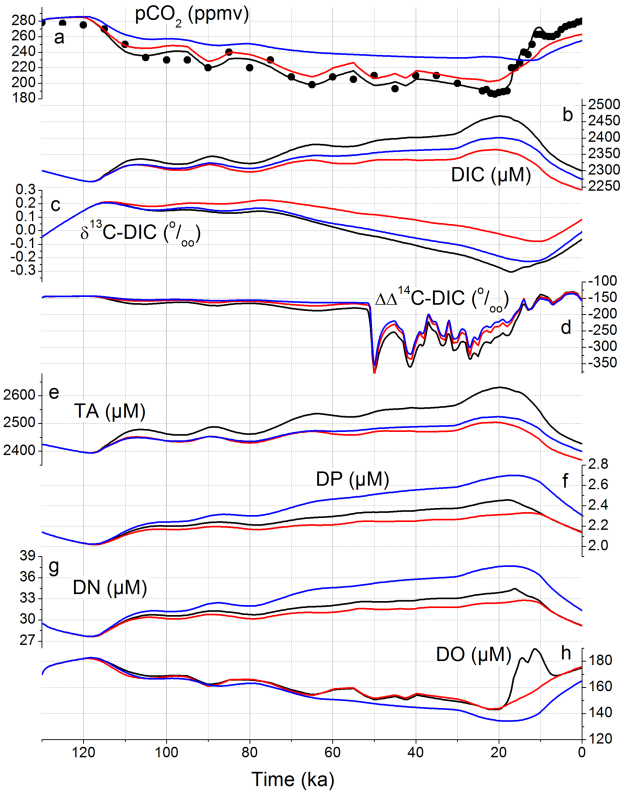

Figure 5. Model results for the standard case (simulation STD, black lines), for constant circulation (simulation STD-CC, red lines), and constant circulation and nutrient utilization (simulation STD-CC-CN, blue lines). **(a)** Atmospheric pCO_2, dots indicate ice-core data (Monnin et al., 2001; Petit et al., 1999; Monnin et al., 2004); **(b–h)** global mean seawater concentrations and isotopic compositions: **(b)** dissolved inorganic carbon (DIC); **(c)** $\delta^{13}C$ of DIC; **(d)** difference between radiocarbon in seawater DIC and atmospheric CO_2 ($\Delta\Delta^{14}C\text{-DIC} = \Delta^{14}C\text{-DIC-}\Delta^{14}C\text{-}CO_2$); **(e)** total alkalinity (TA); **(f)** dissolved phosphorus (DP); **(g)** dissolved reactive nitrogen (DN); **(h)** dissolved oxygen (DO).

The major new component included in our Earth system model is a comprehensive formulation of shelf processes and sea-level effects. Appendix B explains in detail how sea-level change affects fluxes at continental margins and how these effects are considered in the model. The full model code is available from the first author on request.

3 Results and discussion

The model was run over a period of 130 kyr to simulate the behaviour of the global system over one full glacial cycle. Simulations start at 130 ka with modern (pre-human) tracer distributions applied as initial values. The standard model run (STD) considers all effects induced by sea-level change,

Table 1. Controls on atmospheric pCO_2 and mean dissolved carbon and phosphorus concentrations in the global ocean.

Simulation	pCO_2 at 21 ka in ppmv	pCO_2 at 0 ka in ppmv	DIC at 21 ka in µM	DIC at 0 ka in µM	DP at 21 ka in µM	DP at 0 ka in µM
STD (standard simulation)	190	279	2465	2300	2.44	2.14
STD with constant SST	206	275	2453	2289	2.48	2.15
STD with constant salinity	185	291	2466	2301	2.44	2.14
STD with constant salinity and constant ocean volume	177	281	2409	2310	2.41	2.16
STD with constant riverine DP flux	240	345	2564	2430	2.16	1.98
STD with constant rates of chemical weathering	193	268	2355	2202	2.15	1.98
STD with constant depositional area for P burial	263	367	2599	2478	2.03	1.95
STD with constant depositional area for POC burial	129	180	2132	1925	2.42	2.07
STD with constant burial rate of neritic carbonates	200	277	2437	2291	2.46	2.15
STD-CC-CN	234	255	2400	2273	2.68	2.30
STD with constant AMOC	200	262	2381	2233	2.49	2.12
STD-CC	203	263	2364	2240	2.31	2.14

changes in ocean circulation, and nutrient utilization, that is the full model forcing as defined in Figs. 3 and 4. Additional simulations were performed to better understand the controls on atmospheric pCO_2 and the chemical and isotopic composition of seawater. Simulation STD-CC was run with constant circulation – that is, all water fluxes were maintained at the Holocene level (upper panel of Fig. 2, Table A3) over the full model period – whereas simulation STD-CC-CN was performed with the Holocene circulation field and constant nutrient utilization.

3.1 Atmospheric pCO_2

The pCO_2 trend recorded in ice cores (Monnin et al., 2001, 2004; Marcott et al., 2014; Petit et al., 1999) was well reproduced by the standard simulation (Figs. 5a and 7a). Over the last interglacial, simulated pCO_2 increased from an initial value of 280 ppmv at 130 ka to 285 ppmv at 120 ka (Fig. 5a). This increase was accompanied by a decline in nutrient concentrations (Fig. 5f–g) and export production (Fig. 6d), supported by the high sea-level stand promoting burial of phosphorus and benthic denitrification in continental margin sediments. Over the subsequent glacial period, simulated pCO_2 declined due to sea-level fall, enhanced nutrient utilization in the Southern Ocean, and the decline in deep ocean ventilation until 21 ka, when a pCO_2 minimum of 190 ppmv was reached (Fig. 7b). The simulated glacial pCO_2 drawdown was discontinuous, marked by several steps and turning points (Fig. 5a). Major minima in atmospheric pCO_2 occurred at 90 ka (220 ppmv) and 65 ka (198 ppmv). Both of them are well documented in the ice-core record (Fig. 5a) and accompanied by maxima in nutrient utilization (Fig. 4e) and minima in sea-level (Fig. 3a). Sea-level fall and nutrient utilization, thus, may have driven most of the glacial pCO_2 decline. Moreover, they may have induced major turning points in the glacial pCO_2 record.

At constant ocean circulation and nutrient utilization (simulation STD-CC-CN), simulated pCO_2 declined to a LGM value of 234 ppmv (Fig. 5a). Additional simulations based on the standard simulation STD helped us to specify the driving forces for this decline (Table 1). To study their effect on pCO_2 we suppressed the temporal changes of individual variables. A first simulation test was based on the assumption of constant modern sea surface temperatures (SSTs). It showed that the glacial decline in global mean SST by ca. 2 °C (Schmittner et al., 2011) induced a pCO_2 decline by 16 ppmv since the solubility of CO_2 in surface waters was enhanced under low temperatures (compare rows 1 and 2 in Table 1). In a second simulation, salinity was set constant, while the other model parameters varied as defined in the STD simulation. Accordingly, the peak glacial increase in salinity induced a relative atmospheric pCO_2 rise by 5 ppmv by lowering the solubility of CO_2 in surface waters (Table 1). In a third test, both salinity and the volume of the ocean boxes were kept constant over time. Changes in these parameters induced an LGM pCO_2 rise by 13 ppmv (Table 1), illustrating that the contraction of the ocean volume during glacial sea-level low-stands reduced the ocean's capacity to sequester atmospheric CO_2. In summary, the model runs confirmed previous estimates (Broecker, 1982b) showing that the net effect of SST, volume, and salinity changes on glacial pCO_2 is small (decrease by 3 ppmv). Thus, other processes need to be invoked to explain the large glacial drawdown of atmospheric CO_2 simulated by model run STD-CC-CN.

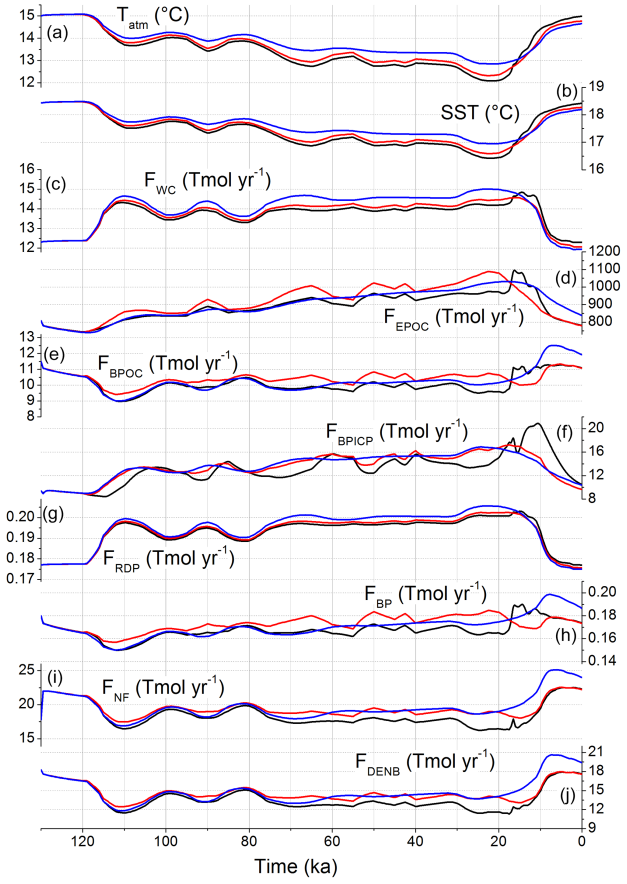

Figure 6. Model results for simulations STD (black lines), STD-CC (red lines), and STD-CC-CN (blue lines). **(a)** Global mean atmospheric near-surface temperature (T_{atm}); **(b)** global mean sea surface temperature (SST); **(c–j)** global rates: **(c)** carbonate weathering (F_{WC}); **(d)** marine export production of POC (F_{EPOC}); **(e)** POC burial (F_{BPOC}); **(f)** burial of pelagic carbonate (F_{BPICP}); **(g)** riverine flux of dissolved phosphorus (F_{RDP}); **(h)** burial of marine phosphorus (F_{BP}); **(i)** nitrogen fixation (F_{NF}); **(j)** benthic denitrification (F_{DENB}).

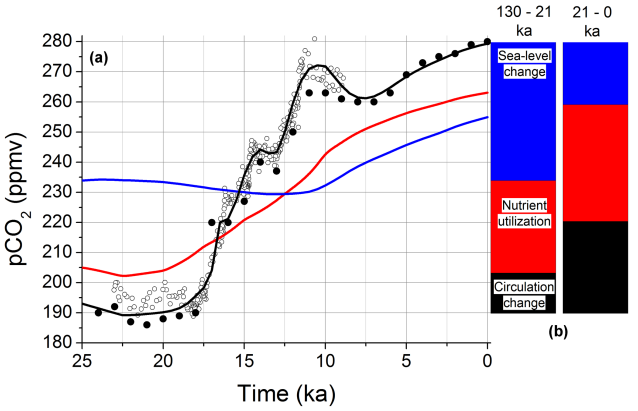

Figure 7. Atmospheric pCO_2 over the last 25 kyr. **(a)** Model results for simulations STD (black line), STD-CC (red line), and STD-CC-CN (blue line); solid dots indicate ice-core data by Monnin et al. (2001, 2004) while ice-core data reported in Marcott et al. (2014) are shown as open circles; **(b)** relative contribution of sea-level change (blue), nutrient utilization (red), and ocean circulation changes (black) to pCO_2 model results; the left-hand column shows contributions to the glacial pCO_2 drawdown (51 % induced by sea-level fall, 34 % by enhanced nutrient utilization, 15 % by changes in ocean circulation); the right-hand column indicates the driving forces for the deglacial pCO_2 rise (23 % induced by sea-level rise, 43 % by decrease in nutrient utilization, 34 % by changes in ocean circulation).

Changes in the flux of dissolved phosphorus (DP) exert large effects on pCO_2, since DP is the ultimate limiting nutrient of the model ocean (Menviel et al., 2012). Neglecting the glacial increase in the weathering of P-bearing solids is raising the LGM pCO_2 value by 50 ppmv (Table 1, rows 5 vs. 1). Most of the P released during chemical weathering originates from apatite, a mineral equally occurring in all rock types (sedimentary, magmatic, and metamorphic). Thus, we assume that the P weathering rate is proportional to the total weathering rate – that is the sum of carbonate, POC, and silicate weathering (Wallmann, 2014). During the glacial, total weathering increased due to the weathering of exposed shelf $CaCO_3$ and POC (Munhoven, 2002; Wallmann, 2014). This rise led to the increase in P weathering simulated in the model. However, a further simulation shows that the overall pCO_2 change induced by chemical weathering of silicate, POC, $CaCO_3$, and P is small (decrease by 3 ppmv) because the glacial CO_2 drawdown induced by P and $CaCO_3$ weathering was largely compensated by the CO_2 release induced by POC weathering (Table 1, STD run with constant rates of chemical weathering). Applying very high molar C : P ratios for POM in shelf sediments (ca. 200), it was previously calculated that shelf weathering resulted in a net increase rather than decrease in atmospheric pCO_2 (Ushie and Matsumoto, 2012). However, most of the phosphorus in shelf sediments and riverine particles is not organic but bound in other reactive, inorganic phases such as carbonate-fluoro-apatite (Berner and Rao, 1994) which release DP when exposed to weathering (Ruttenberg, 1992; Ruttenberg and Berner, 1993). Thus, the global mean atomic ratio of POC over reactive P in shelf sediments is lower than the C : P ratio of marine organic matter (Baturin, 2007; Wallmann, 2010). Hence, the glacial weathering of shelf sediments induced a small drop rather than a rise in LGM pCO_2 (Table 1).

By contrast, a stronger effect results from testing the glacial decrease in depositional areas at continental margins, as revealed by a simulation that ignores the glacial decline in P burial and reveals a glacial pCO_2 rise by 73 ppmv (Table 1) with respect to the standard case due to the decline in DP concentration and export production. An additional simulation with constant depositional area for POC burial resulted in a pronounced drawdown of both atmospheric pCO_2

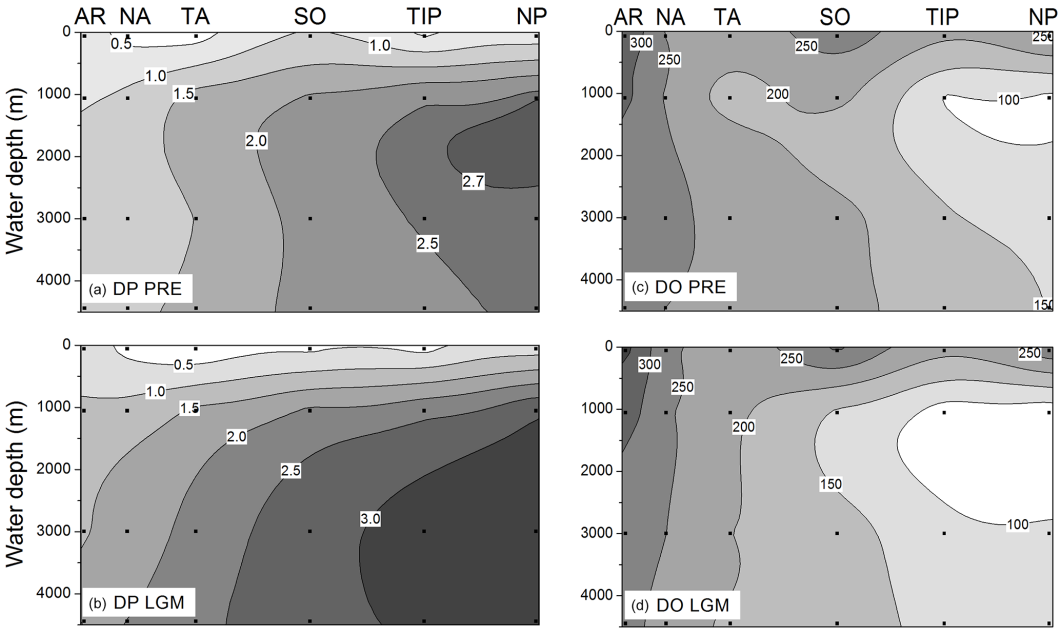

Figure 8. Concentrations (in µM) of dissolved phosphorus (DP) and oxygen (DO) in the pre-anthropogenic modern ocean (PRE, model results for 0 ka, **a**: DP, **c**: DO) and during the LGM (model results for 21 ka, **b**: DP, **d**: DO, Table C4). The contour plots shown here and in Figs. 9 and 11 are based on concentrations calculated in simulation STD for each of the 24 ocean boxes (indicated as grid points).

(by 61 ppmv) and DIC since POC burial at continental margins served as a major sink for CO_2 and DIC in the model system (Table 1). Changes in the burial of neritic carbonates had a less drastic effect on atmospheric pCO_2 (change by 10 ppmv, Table 1) since they were mitigated by carbonate compensation at the deep-sea floor. Thus, the response of the model system to sea-level change was dominated by changes in the burial of P and POC at continental margins. The glacial drop in atmospheric pCO_2 that was induced by a decline in P burial and a corresponding rise in export production was moderated by a coeval drop in POC burial at continental margins. The overall effect was an enhanced sequestration of CO_2 in the glacial deep ocean accompanied by a decrease in sedimentary POC accumulation. Accordingly, most of the glacial pCO_2 decline in simulation STD-CC-CN was driven by the glacial steepening of ocean margins and the resulting expansion of the DP inventory. This conclusion is consistent with the results of previous experiments conducted with more evolved Earth system models showing a strong pCO_2 drawdown in response to an increase in the oceanic phosphate inventory (Tschumi et al., 2011; Menviel et al., 2012).

The glacial pCO_2 value dropped by 31 ppmv (from 234 to 203 ppmv) upon enhanced nutrient utilization (difference between simulations STD-CC-CN and STD-CC). This decrease was amplified by the glacial sea-level fall since the nutrient reservoir that was unlocked by the enhanced utilization in the glacial Southern Ocean was enlarged as a result of glacial marine regression. The remaining portion of the interglacial-to-peak glacial pCO_2 drop by 13 ppmv down to the final LGM value of 190 ppmv was induced by ocean dynamics (difference between simulation STD and STD-CC). Atmospheric pCO_2 rose by 10 ppmv, when all water fluxes between the Atlantic and the Southern Ocean were maintained at their Holocene level over the entire model period (simulation STD with constant AMOC, Table 1). The glacial AMOC shoaling (Fig. 4a–b) thus contributed 10 ppmv to the simulated LGM decline. This effect can be attributed to enhanced CO_2 storage in the deep Atlantic (> 2000 m water depth) which was less ventilated under glacial conditions, since the formation of northern deep waters was greatly diminished and replaced by southern-source waters enriched in DIC. Thus additional DIC was stored in the glacial deep ocean (Ganopolski et al., 2010; Skinner, 2009; Sarnthein et al., 2013). The glacial decrease in water fluxes between the deep Southern Ocean and Tropical Indo-Pacific applied in the model (Fig. 2) likewise supports further sequestration and storage of CO_2 in the deep ocean and the glacial drawdown of atmospheric pCO_2. The circulation changes employed to simulate LGM conditions (Fig. 2) led to a reduction in the global water exchange across the 2000 m depth horizon from a modern amount of 45 Sv down to 31 Sv at 21 ka. This corresponds to an increase in the average residence time of water in the deep ocean (> 2000 m) from 470 years in the modern ocean to 680 years during the LGM where the residence time is calculated as the ratio of the deep ocean volume (6.65×10^{17} m^3 at > 2000 m) and the global vertical water fluxes across 2000 m. The glacial increase in residence time

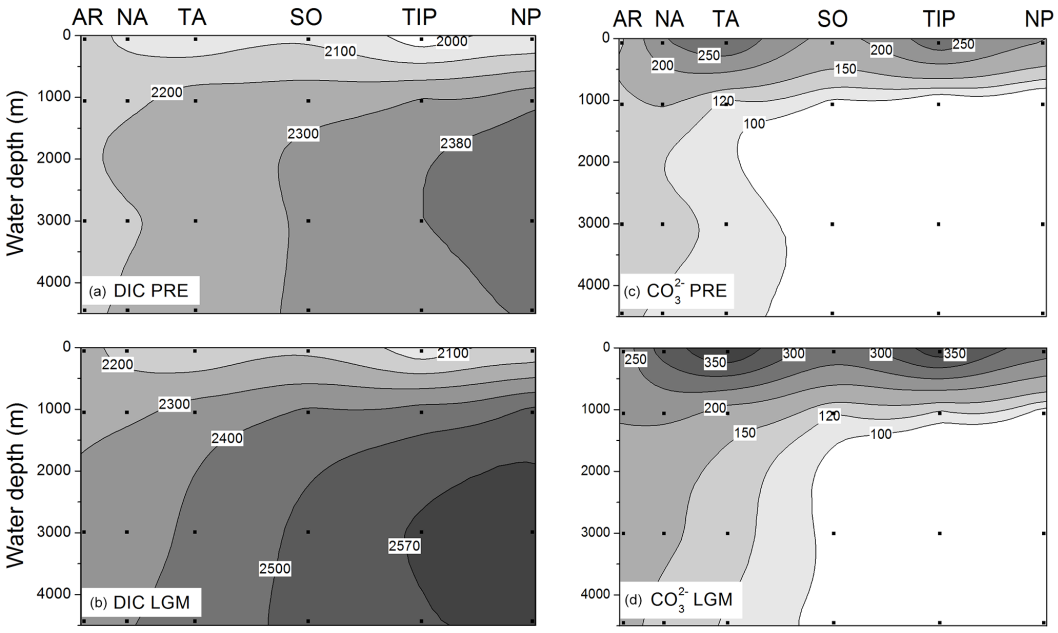

Figure 9. Concentrations of dissolved inorganic carbon (DIC in µM) and carbonate ions (CO_3^{2-} in µmol kg^{-1}) in the pre-anthropogenic modern ocean (PRE, model results for 0 ka, **a**: DIC, **c**: CO_3^{2-}) and during the LGM (model results for 21 ka, **b**: DIC, **d**: CO_3^{2-}, Table C4). See legend of Fig. 8 for further information.

by 210 years may be compared to the 600-year increase reconstructed from benthic radiocarbon data (Sarnthein et al., 2013). We suggest that the difference between these two estimates is related to the elevated production rate of radiocarbon in the glacial atmosphere and changes in carbon cycling affecting the marine radiocarbon budget (Sect. 3.4).

A stepwise increase in pCO_2 was simulated over the deglaciation (Fig. 7). The first step occurred from 18.5 to 16.3 ka when the simulated pCO_2 rose rapidly from 193 to 220 ppmv. A second step followed at 15.9–14.1 ka with a pCO_2 rise from 222 to 244 ppmv, and a third step at 13.0–10.8 ka with a strong increase from 243 to 272 ppmv. The first step was driven by the rapid drop in nutrient utilization at the glacial termination (Fig. 4e) and the ventilation of intermediate and deep water masses in the North Pacific during H1 (Figs. 4d and A2). The second and third steps were driven by the Southern Ocean where CO_2 was released into the atmosphere due to the abrupt decline in stratification and the further decrease in nutrient utilization (Fig. 4d–e). In major parts of the Southern Ocean these steps coincide with maxima in opal accumulation indicating enhanced upwelling (Anderson et al., 2009). The pCO_2 drawdown from 10 to 8 ka reflects a recovery of the ocean system from the antecedent ventilation pulse in the Southern Ocean centred at 11.5 ka (Fig. 4d). According to our model, the ventilation pulse removed CO_2 from the ocean interior, enhanced the O_2 content of the deep ocean, and diminished the vertical DIC and O_2 gradients. The subsequent restoration of the vertical DIC gradient induced the pCO_2 decline observed in the model from 10 to 8 ka. The biological pump needed about 2 kyr to reestablish the vertical DIC gradient due to the large inventory of DIC in the deep ocean. Sea-level change was not uncovered as a major driver for the rapid deglacial pCO_2 rise since the long residence times of DP (13 kyr) and TA (77 kyr) inhibit fast inventory changes in the global ocean (Menviel et al., 2012; Wallmann, 2014). By contrast, the pCO_2 increase over the Holocene (8–0 ka), which is closing the glacial cycle, may have been driven by a high sea-level stand inducing a gradual and slow decline in marine DP and TA inventories.

In our model about equal portions of the extreme deglacial carbon flux are triggered by changes in circulation and nutrient utilization in the Southern Ocean (Fig. 7). However, this model outcome is not well constrained because the lack of both proxy data and physical process understanding impedes an unequivocal determination of the magnitude of these changes in the Southern Ocean.

3.2 Dissolved nutrients and oxygen

The standing stock of DP in the global ocean rose under glacial conditions since P burial was diminished by the decrease in depositional area located at shallow water depths (Fig. 6h) while chemical weathering was promoted by the exposure of shelf sediments (Fig. 6g). Most of the glacial DP rise found in our simulations was induced by the glacial steepening of ocean margins reducing the burial of P in margin sediments (Table 1, Fig. 1, Appendix B). Vice versa, enhanced utilization in the Southern Ocean induced a strong

decrease in glacial DP stocks since more DP was taken up by phytoplankton to be drawn down and finally buried in marine sediments (simulations STD-CC vs. STD-CC-CN, Figs. 5f, 6d, h), while the glacial DP stock was largely restored by changes in ocean dynamics (simulations STD vs. STC-CC, Fig. 5f) separating the large nutrient pool in the deep ocean from the surface layer. The spatial distribution of DP in the global ocean reflects the export of POM by the biological pump and ocean circulation. The overall pattern, that is a strong vertical gradient between depleted surface waters and enriched deep water masses and a significant horizontal gradient between the deep North Atlantic and North Pacific, was maintained over the glacial cycle (Fig. 8). However, the vertical DP gradient was amplified over the LGM due to enhanced utilization and the decrease in deep ocean ventilation. Reactive P accumulation rates in marine sediments can be used to validate our model results. A global compilation of these data confirmed that P accumulation in shelf sediments decreased drastically under glacial conditions (Tamburini and Föllmi, 2009). The resulting decline in global P burial induced an increase in the glacial DP inventory by 17–40 % (Tamburini and Föllmi, 2009) as predicted by our model. Cd / Ca ratios in LGM sediments from the Atlantic Ocean (Boyle and Keigwin, 1982) and δ^{13}C records (Duplessy et al., 1988; Sarnthein et al., 1994; Oliver et al., 2010) suggest a steepening of the vertical DP gradients broadly consistent with our model results.

The dissolved oxygen (DO) content of the global ocean decreased under glacial conditions due to the decline in deep ocean ventilation and increase in export production (Fig. 5h). In contrast, it recovered and peaked over the deglaciation since ocean ventilation was enhanced in the Southern Ocean and the North Pacific. The spatial distribution of DO changed significantly under LGM conditions (Fig. 8). Concentrations declined at > 2000 m water depth due to the decrease in ocean ventilation and increase in export production while glacial cooling induced a small DO rise in surface waters. The DO minimum in intermediate waters of the Indo-Pacific expanded and spread into the deep ocean under glacial conditions. The lowest value was calculated for the intermediate water box of the North Pacific where the DO concentration declined to 69 µM at 21 ka. The glacial DO decrease in the deep ocean is consistent with a large data set showing that deep waters below 1500 m water depth were significantly depleted in the LGM over all major ocean basins (Jaccard and Galbraith, 2012). The glacial oxygen depletion in the intermediate Indo-Pacific (76 µM during the LGM vs. 96 µM in the modern ocean) seems to be at odds with the geological record which shows that OMZs located in the tropical ocean were better ventilated under glacial conditions (Altabet et al., 1995). This discrepancy may probably arise from the spatial resolution of the box model that is too coarse to resolve OMZs. Moreover, all sediment cores that have been used to reconstruct the oxygen conditions in glacial intermediate waters were taken at continental margins (Jaccard and Galbraith, 2012) while tracer concentrations in the model boxes are basin-wide mean values reflecting open ocean rather than continental margin conditions.

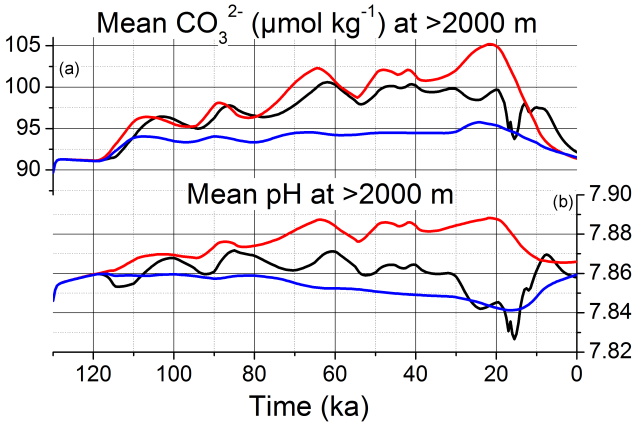

Figure 10. Global mean carbonate ion concentrations **(a)** and pH values **(b)** below 2000 m water depth for simulations STD (black line), STD-CC (red line), and STD-CC-CN (blue line).

The glacial oxygen decline simulated in the model had no significant effect on other model parameters since the oxygen level stayed above the threshold values for diminished phosphorus burial (20 µM) in all ocean boxes (Wallmann, 2010). It was only benthic denitrification at the deep-sea floor that was enhanced by the glacial oxygen depletion in bottom waters and rising export production (Bohlen et al., 2012). Nevertheless, the global rate of benthic denitrification calculated in simulation STD decreased under glacial conditions (Fig. 6j) since ocean margins retreated into steeper terrain such that less nitrate was consumed on the continental shelf. Nitrogen fixation was assumed to increase when the DN / DP ratio in the surface ocean fell below the N / P ratio in exported POM (Eq. A8). Nitrogen fixation thus traced the temporal evolution of benthic denitrification (Fig. 6i–j). This negative feedback mechanism (Tyrrell, 1999; Redfield, 1958) maintained the simulated DN / DP ratio close to its modern value over the entire glacial cycle. The DN inventory peaked during the LGM where it exceeded the modern value by 16 %. A similar increase in the LGM nitrate inventory (10–30 %) and glacial decline in denitrification and nitrogen fixation was simulated with a box model constrained by the marine δ^{15}N record (Deutsch et al., 2004).

3.3 Dissolved inorganic carbon, carbonate ion concentrations, and δ^{13}C of dissolved inorganic carbon

In the standard case (STD) the global mean seawater concentrations of dissolved inorganic carbon (DIC) and total alkalinity (TA) decreased over the last interglacial, attained a minimum at its end (2267 and 2394 µM at 118.5 ka, respectively), increased over the glacial up to a maximum prior to

the glacial termination (2467 and 2631 µM at 19.5 ka), and decreased again over the Holocene (Fig. 5b and e). On the basis of our model runs these trends were mainly driven by sea-level change that controlled the burial of neritic carbonate (Fig. 3d) and POC (Fig. 6e), and the rates of POC and carbonate weathering by shelf exposure (Figs. 3h and 6c). The glacial DIC and TA rise was mitigated by nutrient utilization enhancing marine export production and carbon burial (compare simulations STD-CC-CN and STD-CC in Figs. 5 and 6). In turn, it was amplified by the glacial decrease in deep ocean ventilation, a reduced turnover rate that also implied a decrease in marine export production, POC burial, and pelagic carbonate accumulation (STD-CC vs. STD). Considering changes in ocean volume by about 3 % (Fig. 3b), the increase in DIC over the last glacial (118.5–19.5 ka) translates into a mean DIC accumulation rate of 1.70 Tmol yr^{-1}. By comparison, the CO_2 uptake from the atmosphere as calculated from the glacial rate of pCO_2 decline amounts to 0.17 Tmol yr^{-1}. Thus, only 10 % of the glacial DIC rise was induced by CO_2 uptake from the atmosphere. According to our model, the glacial demise of neritic carbon pools (carbonate and POC) was the major forcing of the DIC rise, while the sequestration of atmospheric CO_2 only was of minor importance for the glacial change in seawater composition. Most of the excess DIC accumulating in the glacial ocean originated from exposed shelf carbonate and POC and from riverine DIC which was not buried due to the contraction of depositional areas at ocean margins. The accumulation of TA and DIC in the deep ocean (Fig. 9) was corroborated by a change in Atlantic deep water chemistry. As outlined above, this LGM ocean basin was filled with corrosive southern-source waters compromising the preservation of carbonates at the deep-sea floor and diminishing the rate of pelagic carbonate burial.

The global mean concentration of carbonate ions (CO_3^{2-}) in the deep ocean (> 2000 m) rose over glacial times in simulation STD due to the decline in neritic carbonate burial and dropped over the deglaciation, at least in part, due to the recovery of neritic carbonate deposition (Fig. 10a). The glacial CO_3^{2-} rise was mitigated by the decline in deep ocean ventilation and increase in ocean productivity promoting the sequestration of CO_2 in the deep ocean. Interestingly, deep ocean pH and CO_3^{2-} trends diverged during the transition into the LGM (Fig. 10a–b) – that is, pH dropped while CO_3^{2-} was maintained at a constant level over this period (30–20 ka). Due to this divergence, the late glacial pH was lower (that is, more acidic) than the modern value, while the CO_3^{2-} concentration exceeded the modern concentration in ocean deep waters. This apparent discrepancy may be explained by the fact that alkalinity and DIC were strongly elevated in late glacial seawater (Fig. 5b and e) thereby enhancing the concentrations of both H^+ and CO_3^{2-} ions with respect to the pre-industrial modern ocean. The deglacial CO_3^{2-} minimum is related to ventilation pulses in the Southern Ocean and North Pacific employed in the model. Export production of $CaCO_3$ and pelagic carbonate burial were enhanced by these upwelling events and removed dissolved CO_3^{2-} from the global ocean. The Holocene was marked by a continuous CO_3^{2-} decline probably induced by the high sea-level stand promoting neritic carbonate burial.

The strong enrichment of dissolved CO_3^{2-} in glacial surface waters was induced by the decline in atmospheric pCO_2 (Fig. 9). According to our standard simulation, these CO_3^{2-} concentrations exceeded Holocene values down to water depths of 1000 m, likewise at northern high latitudes where deep-water formation transmitted the signature of glacial surface waters into the ocean's interior. The carbonate ion concentration was almost constant over the entire Indo-Pacific at > 1000 m water depth since the strong increase in DIC (Fig. 9) was balanced by a corresponding TA rise. These model results well compare with those of B / Ca ratios in benthic foraminifera which probably record CO_3^{2-} changes in ambient bottom waters (Yu et al., 2008, 2013). The model is consistent with glacial to interglacial changes in deep-sea CO_3^{2-} reconstructed from this proxy (Table C1 in Appendix C). The only deviation occurs at > 4 km water depth in the Atlantic where the model predicts elevated LGM values while the data show a glacial CO_3^{2-} depletion (Table C1), possibly the result of a strong east–west gradient in bottom water chemistry not resolved yet by the B / Ca data that accordingly may not be fully representative for the Atlantic at large.

The glacial distribution pattern of δ^{13}C-DIC values calculated in the standard simulation (Fig. 11) is consistent with observations (Oliver et al., 2010) because glacial δ^{13}C-DIC data were employed to define the LGM circulation pattern (Sect. 2, Table A5 in Appendix A). In all simulations global mean δ^{13}C-DIC values mirror inversely DIC concentrations (Fig. 5b–c) getting depleted with rising DIC and vice versa. This anti-correlation is linked to the turnover of POC being strongly depleted in ^{13}C as compared to average seawater. The glacial demise of the sedimentary POC pool, induced by the weathering of exposed shelf sediments and the decline in depositional areas along continental margins, contributed significantly to the glacial DIC rise and affected the isotopic evolution of seawater (Broecker, 1982b; Wallmann, 2014). The glacial δ^{13}C-DIC depletion was widely ascribed to a glacial loss of terrestrial biomass (Shackleton, 1977; Köhler and Fischer, 2004). However, our model can reproduce almost the entire glacial shift to depleted δ^{13}C-DIC values recorded in benthic foraminifera (0.34 ± 0.19 ‰; Peterson et al., 2014) without invoking any net changes in terrestrial biomass (Table A5). This outcome is consistent with results of a new model study suggesting that the rise in carbon buried in permafrost and under ice largely compensated for the decline in peat, soil, and biomass carbon over the LGM (Brovkin and Ganopolski, 2015).

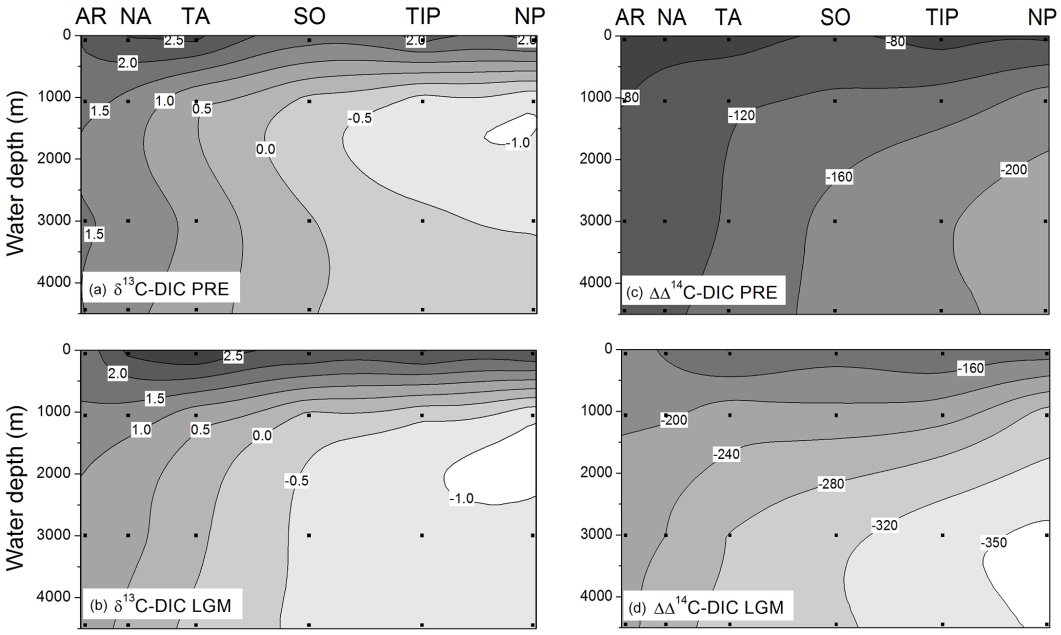

Figure 11. Isotopic composition of dissolved inorganic carbon (DIC) in the global ocean. δ^{13}C of dissolved inorganic carbon (δ^{13}C-DIC in ‰) and radiocarbon composition of dissolved inorganic carbon ($\Delta\Delta^{14}$C-DIC in ‰) in the pre-anthropogenic modern ocean (PRE, model results for 0 ka, **a**: δ^{13}C-DIC, **c**: $\Delta\Delta^{14}$C-DIC) and during the LGM (model results for 21 ka, **b**: δ^{13}C-DIC, **d**: $\Delta\Delta^{14}$C-DIC, Table C4). $\Delta\Delta^{14}$C-DIC values represent the difference between seawater Δ^{14}C-DIC and the atmospheric value (0 ‰ for the pre-anthropogenic modern, +446 ‰ for the LGM). See legend of Fig. 8 for further information.

3.4 Radiocarbon

Atmospheric Δ^{14}C-CO_2 was forced to follow the IntCal13 values derived from the geological record by varying the ^{14}C-production rate in the atmosphere (Appendix A, Sect. A8). The ^{14}C production rate was calculated for each time step considering the ^{14}C transfer from the atmosphere to the oceans and changes in the inventories of atmospheric CO_2 and ^{14}C-CO_2. Δ^{14}C-CO_2 and the model-derived difference between global mean Δ^{14}C-DIC and atmospheric Δ^{14}C-CO_2 ($\Delta\Delta^{14}$C-DIC = Δ^{14}C-DIC – Δ^{14}C-CO_2) were anti-correlated, since the ^{14}C uptake from the atmosphere was insufficient to raise the radiocarbon content of the model ocean up to the level of elevated Δ^{14}C-CO_2 values attained during periods of strong atmospheric radiocarbon production (Figs. 5d, 4g, and 12). This anti-correlation was also observed in an additional simulation (Fig. 12b) where the carbon cycle and ocean circulation were maintained at a steady state representing Holocene boundary conditions, whereas Δ^{14}C-CO_2 values were forced to follow the IntCal13 record. In further steady-state simulations the radiocarbon production rate in the atmosphere was held constant over time while the carbon cycle operated in a Holocene steady-state mode with a constant pCO_2 value of 280 µatm. These model runs show that the steady-state $\Delta\Delta^{14}$C-DIC values attained after about 100 kyr simulation time decreased with increasing production rate (Appendix C, Table C2). As previously shown, changing production rates of radiocarbon in the atmosphere may affect the difference between Δ^{14}C values in planktonic and benthic foraminifera (Adkins and Boyle, 1997) and the contrast between atmospheric and marine Δ^{14}C values (Franke et al., 2008). However, these effects were regarded as transient features induced by a slow ^{14}C transfer from the atmosphere into the ocean. In contrast, the results of our steady-state model suggest that ^{14}C depletion of the ocean during periods of elevated atmospheric ^{14}C production can be a permanent steady-state feature (Table C2), a conclusion further substantiated by a simple steady-state model presented in Appendix D.

The standard simulation STD yielded a mean ocean $\Delta\Delta^{14}$C-DIC of −270 ‰ for the LGM (21 ka) and −152 ‰ at 0 ka corresponding to a glacial $\Delta\Delta^{14}$C-DIC decline by 118 ‰. The simulations depicted in Fig. 12b show that multiple processes contributed to the ^{14}C glacial depletion of the ocean with respect to the atmosphere. These include the glacial changes in deep ocean ventilation, sea-level, nutrient utilization, and atmospheric radiocarbon production. The $\Delta\Delta^{14}$C-DIC decline observed upon sea-level fall in part was induced by the glacial decline in sedimentary carbon pools adding fossil carbon to the global ocean. Glacial changes in ocean circulation contributed to the $\Delta\Delta^{14}$C-DIC decline since the glacial demise of ventilation across the 2000 m depth horizon isolated the deep ocean from the atmosphere. However, the simulations suggest that changes in ocean ventilation possibly were responsible for less than one-third of

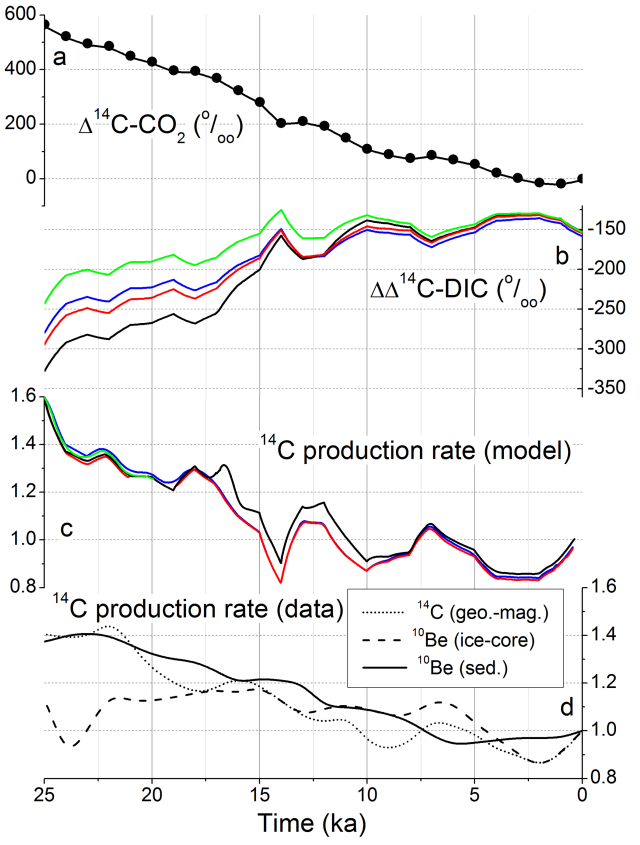

Figure 12. Radiocarbon values and production rates. **(a)** Atmospheric Δ^{14}C-CO_2; dots are IntCal13 data (Reimer et al., 2013) while the black line shows the values applied in the model runs. **(b)** Marine $\Delta\Delta^{14}$C-DIC values calculated as difference between radiocarbon in seawater DIC and atmospheric CO_2. The results of simulations STD-CC-CN, STD-CC, and STD are indicated as blue, red, and black lines, respectively. The green line indicates the results obtained in a steady-state simulation under Holocene boundary conditions where all variables except atmospheric Δ^{14}C-CO_2 and radiocarbon production rate were kept constant over time. **(c)** Production rates of radiocarbon in the atmosphere calculated in the model runs and normalized to the pre-anthropogenic modern value (1.64 atoms cm^2 s^{-1}). **(d)** ^{14}C production rates calculated from the geo-magnetic record (Laj et al., 2002); ^{10}Be production rate as reconstructed from Greenland ice-core data (Muscheler et al., 2005; Reimer et al., 2013), ^{10}Be production rate as reconstructed from sediment data (Frank et al., 1997); all rates are normalized to their pre-anthropogenic modern values.

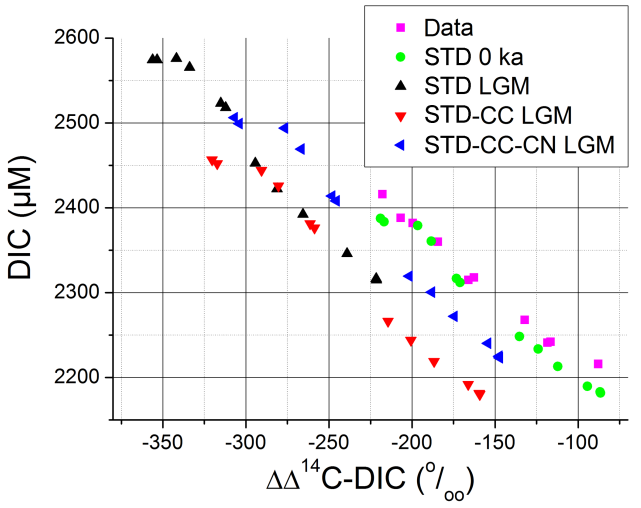

Figure 13. DIC vs. difference between radiocarbon in seawater DIC and atmospheric CO_2 ($\Delta\Delta^{14}$C-DIC) at > 2000 m water depth. Data are mean values for deep water and bottom water boxes derived from water column measurements. Model results are shown for the standard case (STD), for constant circulation (STD-CC), and constant values for circulation and nutrient utilization (STD-CC-CN). LGM refers to model results at 21 ka.

the glacial rise in the radiocarbon contrast between global ocean and atmosphere.

Atmospheric ^{14}C production rates calculated in the model showed the same trends for all simulations (Fig. 12c). They attained very high values at 25 ka and declined over time. The only significant difference between the model runs occurred during the deglaciation. The standard simulation yielded elevated production rates for this period since the rapid ventilation of the deep ocean considered in simulation STD drew radiocarbon from the atmosphere and released ^{14}C-depleted CO_2 into the atmosphere such that the production rate was enhanced to maintain atmospheric Δ^{14}C-CO_2 at the deglacial level documented by IntCal13 (Fig. 12a). Our model results may support the hypothesis that a significant fraction of the Δ^{14}C-CO_2 record is controlled by changes in atmospheric radiocarbon production (Köhler et al., 2006; Broecker et al., 2004). However, in contrast to our model approach various authors have proposed that most of the Δ^{14}C-CO_2 record can be explained by changes in glacial ocean dynamics and carbon cycling without invoking significantly elevated rates of atmospheric radiocarbon production (Muscheler et al., 2005; Robinson et al., 2005). The Holocene trends calculated in the model are similar to those observed in the ^{10}Be ice-core record (Muscheler et al., 2005) and derived from Holocene geo-magnetic data (Laj et al., 2002) while the glacial values are closer to the stacked sedimentary ^{10}Be record (Frank et al., 1997). Various reasons have been evoked to explain the deviations between different records of atmospheric radionuclide production (Köhler et al., 2006). The controversy suggests a clear need to develop a better constrained record of atmospheric ^{14}C production suitable for model validations (Fig. 12d).

The spatial distribution of radiocarbon in the global ocean changed significantly during the LGM (Fig. 11). According to the standard simulation $\Delta\Delta^{14}$C-DIC values were strongly depleted over the entire ocean and reached a minimum of −356 ‰ in North Pacific deep water. Both, vertical and horizontal gradients were strengthened during the LGM. In the modern ocean, marine Δ^{14}C-DIC values are correlated with

DIC concentrations at water depths below 2000 m (Sarnthein et al., 2013). If this correlation also holds for the glacial ocean, glacial $\Delta\Delta^{14}$C-DIC values may be used as a proxy for DIC concentrations in glacial seawater (Sarnthein et al., 2013). The model results show that the correlation was indeed maintained in the glacial ocean and the slope of the correlation was similar for all model runs and time slices (Fig. 13). However, the regression line for glacial conditions was shifted to lower DIC and $\Delta\Delta^{14}$C-DIC values due to changes in ocean carbon cycling and possibly elevated radiocarbon production rates in the glacial atmosphere. Thus $\Delta\Delta^{14}$C-DIC values may serve as a new proxy for DIC concentrations in ancient seawater, if suitable methods are found to correct for the glacial shift observed in the simulations (Fig. 13). The overall LGM pattern calculated in the standard simulation (Fig. 11) compares well with trends derived from the radiocarbon contents of planktonic and benthic foraminifera, even though radiocarbon data indicate strong gradients within ocean basins, which were not resolved by the box model (Appendix C, Table C3). A recent review of glacial $\Delta\Delta^{14}$C-DIC data (Sarnthein et al., 2013) revealed radiocarbon depletions in the deep Atlantic, Southern Ocean, and Indo-Pacific broadly consistent with those calculated by the model. However, the model was not able to reproduce very strong radiocarbon depletions measured at some deep water sites due to its coarse spatial resolution (Table C3). Moreover, it predicts significant ^{14}C-depletions in the Atlantic thermocline which are inconsistent with coral ^{14}C data (Robinson et al., 2005). ^{14}C measurements in foraminiferal shells and corals from the glacial ocean feature strong spatial and temporal variability (Broecker et al., 2004; Sarnthein et al., 2013). More data will help to resolve this variability and constrain the radiocarbon distribution and dynamics of the glacial ocean.

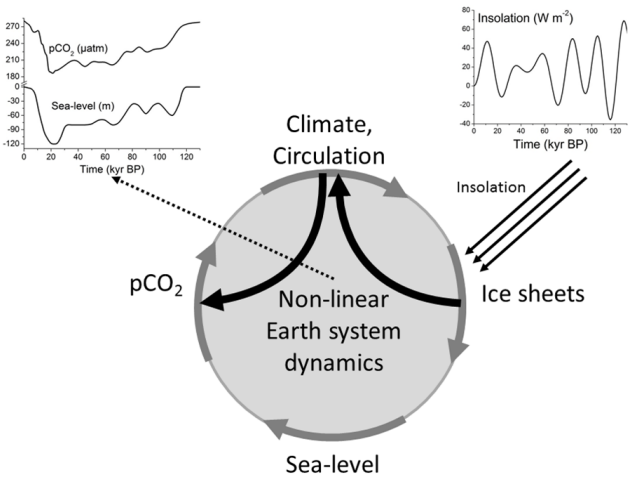

Figure 14. Key elements of the 100 kyr cycle. Summer insolation at high northern latitudes (June insolation at 60° N, diagram in the upper right corner, Berger and Loutre, 1991) affects the growth and melting of continental ice sheets and thereby eustatic sea-level change. The glacial drawdown of atmospheric pCO_2 and its deglacial rise are supported by sea-level change. The cycle is closed by atmospheric pCO_2 affecting global climate and thereby the volume of continental ice sheets. It is accelerated and further strengthened by additional positive feedbacks: ice sheets affect the Earth's albedo and climate while changes in ocean and atmosphere circulation support the glacial pCO_2 drawdown and are largely responsible for the rapid deglacial rise in atmospheric pCO_2. The records of atmospheric pCO_2 and eustatic sea-level change (diagrams in the upper left corner; Monnin et al., 2001, 2004; Petit et al., 1999; Waelbroeck et al., 2002; Stanford et al., 2011) reflect the internal non-linear dynamics of the Earth system and its response to external insolation forcing.

4 Conclusions

For a first time we show model results that are consistent with both the atmospheric pCO_2 record (Figs. 5 and 7) and data on past distribution changes of dissolved oxygen, carbonate, and radiocarbon in the glacial ocean (Figs. 8, 9, 11 and Tables C1 and C3). Atmospheric pCO_2 and the glacial distribution of seawater tracers were not prescribed but calculated as prognostic model variables. Only marine δ^{13}C data were used to parametrize the glacial circulation model. A comprehensive formulation of shelf processes and sea-level effects is a major new component included in our Earth system model. Thus, the conformity between independent proxy data and key model results (atmospheric pCO_2 change over the last 130 kyr, distribution of dissolved oxygen, carbonate, and radiocarbon in the LGM ocean) supports our hypothesis that the glacial sea-level drop induced a decline in atmospheric pCO_2 and a rise in the inventories of nutrients, DIC, and alkalinity in the glacial ocean (Wallmann, 2014). Also, we first show that the slope of DIC vs. radiocarbon observed in the modern deep ocean (Sarnthein et al., 2013) was probably maintained in the glacial ocean (Fig. 13). However, a glacial shift in the intercept now complicates the use of ^{14}C as DIC proxy.

The shelf hypothesis was originally developed to explain the deglacial rise in atmospheric pCO_2 (Broecker, 1982a). In contrast, our model analysis reveals that shelf and sea-level effects were not responsible for this rapid rise but account for a major portion of the slow glacial decline of atmospheric pCO_2 (Figs. 5 and 7). The deglacial sea-level rise induced a decline in nutrient and carbon stocks in the global ocean. However, these stocks changed only slowly due to their large size (Menviel et al., 2012). In contrast to the "early anthropogenic hypothesis" (Ruddiman et al., 2016), we attribute the gradual pCO_2 rise over the Holocene to the slow relaxation of nutrient and carbon stocks promoting CO_2 transfer from the ocean into the atmosphere. The slow relaxation may also be responsible for the imbalance in phosphate and TA sources and sinks observed in the modern ocean (Wallmann, 2010, 2014). Stocks of these chemical species may decline

until today since tens of thousands of years may be needed to draw down the dissolved P and TA inventories from their peak values attained over the last glacial maximum.

According to standard Milankovitch theory (Milankovitch, 1941), variations in summer insolation at high latitudes (Berger and Loutre, 1991) cause waxing and waning of northern ice sheets (Fig. 14). Most of the global climate change over a glacial cycle is thus believed to be driven by northern summer insolation and ice sheet dynamics (Denton et al., 2010). However, it has always been difficult to explain why atmospheric pCO_2 declined over glacial periods and how this drop was connected to the buildup of large continental ice sheets. The sea-level effects explored in this paper provide the missing link between glacial ice sheet and pCO_2 dynamics. The sea-level-driven pCO_2 decline was amplified by a decrease in deep ocean ventilation, a decline in sea surface temperature, and enhanced nutrient utilization. These additional changes were driven by a combination of greenhouse gas, albedo, and insolation forcing (Fig. 14). Glacial terminations occurred when summer insolation increased at northern latitudes (Raymo et al., 1997), ice sheets reached a critical size (Denton et al., 2010), and carbonate compensation at the deep-sea floor reversed the declining pCO_2 trend (Wallmann, 2014). The deglacial warming was again driven by greenhouse gas, albedo, and insolation forcing promoting the retreat of continental ice sheets, sea-level rise, ocean ventilation, and the decline in nutrient utilization in a positive feedback mode.

Due to their internal non-linear dynamics, continental ice sheets are able to generate 100 kyr cycles with a slow glacial expansion and rapid deglacial contraction of ice volume under Milankovitch forcing even though insolation oscillates on much shorter timescales (Imbrie and Imbrie, 1980; Abe-Ouchi et al., 2013; Ganopolski and Calov, 2011; Pollard, 1983). Positive feedbacks embedded in the global carbon cycle are able to generate a 100 kyr cycle without any form of external forcing when surface temperature, ice volume, sea-level, and ocean circulation are assumed to be controlled by pCO_2 (Wallmann, 2014). Thus, both, continental ice sheets and the global carbon system have the inherent tendency to generate cycles with a length of 100 kyr. They interact via sea-level and pCO_2 change, respond to insolation forcing, control changes in the climate system (surface temperature, ocean and atmospheric circulation) and may generate the 100 kyr cycle dominating late Quaternary climate change.

Appendix A: Model set-up and calibration

A1 Data and procedures for model calibration

Mean tracer concentrations were calculated for each of the model boxes using the GLODAP database for total alkalinity, DIC, ^{13}C-DIC, and ^{14}C-DIC (Key et al., 2004) and the World Ocean Atlas (WOA01) for temperature, salinity, PO_4, NO_3, and O_2 (Conkright et al., 2002). ^{14}C-DIC data were corrected by subtracting the bomb-^{14}C signal and DIC data were corrected for the intrusion of anthropogenic CO_2 (Key et al., 2004), whereas ^{13}C-DIC data were not corrected and are thus affected by ^{13}C-depleted anthropogenic CO_2. The model was run into steady state under pre-anthropogenic boundary conditions and resulting tracer concentrations were compared to data to validate the model output and calibrate the model (Tables A1 and A2, Fig. A1). The pCO_2 value and global export production of particulate organic carbon were used as additional constraints, i.e. the calculated values had to comply with the corresponding observations (ca. 280 µatm and ca. 700–900 Tmol yr^{-1}, respectively, Sarmiento and Gruber, 2006). For these initial model runs, the riverine fluxes to the ocean were enhanced to compensate for the removal fluxes observed in the modern ocean. The atmospheric pCO_2 value was calculated by applying a constant continental CO_2 uptake rate balancing the CO_2 being produced in the modern ocean by carbonate burial and degassing processes (Wallmann, 2014). The isotopic composition of atmospheric CO_2 was maintained at a constant level representative for the pre-human atmosphere ($\delta^{13}C = -6.5$ ‰, $\Delta^{14}C = 0$‰). Water fluxes (Table A3) and parameter values for key biogeochemical processes (Table A4) were varied until pCO_2, global export production, and the tracer distribution fields generated by the steady-state box model were consistent with data (Tables A1 and A2, Fig. A1). A good fit was obtained for all tracers except ^{13}C-DIC. Some of the ^{13}C mismatch was induced by anthropogenic ^{13}C which has a strong effect on the observations in the modern ocean but was not considered in the model simulations.

A2 Ocean circulation and tracer transport

Water fluxes between adjacent boxes were calculated by using output of the Opa 8.2 ocean circulation model in the framework of NEMO (Nucleus for European Modelling of the Ocean) to start with a configuration that is dynamically consistent with a 3-D forward ocean model (Madec et al., 1998). NEMO was forced by atmospheric reanalysis data as described in Aumont and Bopp (2006). A more detailed analysis of the resulting large-scale circulation pattern is given in Bordelon-Katrynski and Schneider (2012). The calculation of water exchange was based on horizontal and vertical velocities on the box model grid. In order to consider two-way exchange between the boxes, not only the net transports, but fluxes in both directions (northward/southward, up/down) were taken into account. Water fluxes at the atmosphere–ocean boundary were calculated as residual fluxes balancing the water exchange for each vertical column. Test runs with the box model revealed, however, that tracer distributions calculated with the NEMO-derived water fluxes were inconsistent with tracer data when the NEMO circulation field was applied in the box model. This mismatch was induced by the coarse spatial resolution of the box model and by errors inherent to the NEMO simulations. The NEMO-derived circulation field was, thus, modified to allow for a better fit to the independent observations listed in Tables A1 and A2 and to bring the circulation field in line with other observations and GCM modelling results. Thus, NEMO features a North Atlantic Deep Water (NADW) formation rate of only ca. 10 Sv whereas tracer data (radiocarbon, phosphate, oxygen) constrain this rate at ca. 15 Sv (Broecker et al., 1998). Moreover, NEMO predicts that Antarctic Bottom Water (AABW) upwells in the Indo-Pacific all the way to the thermocline and surface ocean. This pattern is consistent with the "great ocean conveyer" (Broecker, 1991) but in conflict with other more recent ocean models suggesting that deep water ascent occurs in the Southern Ocean rather than in the Indo-Pacific (Sarmiento and Gruber, 2006). These models show that AABW flowing into the Indo-Pacific returns as deep water to the Southern Ocean where it ascends to form intermediate water masses flowing northwards into the major ocean basins (Imbrie et al., 1993; Gnanadesekian and Hallberg, 2002; Marinov et al., 2006). NEMO also predicts an extremely high rate of vertical water exchange in the Southern Ocean across 2000 m water depth of more than 200 Sv. These strong upward and downward water fluxes are inconsistent with tracer observations showing strong vertical gradients between the deep ocean (> 2000 m water depth) and the overlying water masses. The water fluxes derived from NEMO were modified to remove these biases and to provide more realistic water fluxes for the box model (Table A3). The corresponding best-fit water fluxes are bidirectional, i.e. water flows in both directions between each of the adjacent model boxes (Table A3). The net fluxes (Table A3) were calculated as the difference between these opposing fluxes. They represent the meridional overturning circulation (MOC) as implemented in the box model (Fig. 2): NADW is formed in the North Atlantic and Arctic basins at an overall rate of ca. 15 Sv. It flows towards the Southern Ocean where Antarctic Bottom Water (AABW) is formed at a rate of ca. 18 Sv. A minor AABW fraction flows northwards into the Atlantic while most of the AABW is filling the deep basins of the Indo-Pacific at a rate of ca. 16 Sv where it upwells and returns into the Southern Ocean as deep water. Intermediate water formed by deep water ascent in the Southern Ocean flows into the Indo-Pacific at a rate of ca. 14 Sv where it upwells to form surface water flowing back towards the Southern Ocean. Surface waters flowing northward into the Atlantic and returning as NADW to the Southern Ocean are closing the loop. This overall MOC pattern and the corre-

Table A1. Salinity (Sal in PSU), dissolved phosphate, nitrate, and oxygen in model boxes (in µM): Model vs. data. Subscripts: S: surface water (0–100 m), I: intermediate water (100–2000 m), D: deep water (2000–4000m), B: bottom water (> 4000 m).

Box	Sal Data	Sal Model	PO_4 Data	PO_4 Model	NO_3 Data	NO_3 Model	O_2 Data	O_2 Model
AR_S	32.96	33.01	0.84	0.825	6.58	11.1	340.7	349
NA_S	35.55	35.24	0.29	0.325	4.	4.67	257.2	248
TA_S	36.22	36.1	0.31	0.335	3.09	4.19	201.6	212
SO_S	34.5	34.3	1.05	1.08	13.01	14.2	290.3	284
TIP_S	35.03	34.95	0.4	0.447	3.03	4.34	198.9	208
NP_S	33.6	33.59	0.84	0.781	8.15	9.88	276.	263
AR_I	34.83	34.82	0.99	0.961	13.22	13.4	296.7	313
NA_I	35.28	35.05	0.87	1.12	16.29	16.8	238.6	234
TA_I	34.99	34.93	1.63	1.72	25.1	25.5	181.5	169
SO_I	34.58	34.54	1.98	2.05	28.43	29.1	209.7	212
TIP_I	34.68	34.64	2.37	2.43	32.16	34.1	107.1	93.4
NP_I	34.32	34.52	2.75	2.67	38.17	35.7	73.65	90.7
AR_D	34.94	34.87	1.04	1.07	14.69	15	287.	287
NA_D	34.95	34.92	1.18	1.19	18.71	16.9	265.1	257
TA_D	34.92	34.9	1.43	1.54	21.67	21.8	245.5	220
SO_D	34.72	34.76	2.2	2.14	31.32	29.2	203.7	211
TIP_D	34.69	34.75	2.49	2.53	35.5	33.9	145.5	149
NP_D	34.65	34.69	2.73	2.57	38.63	34.1	116.	134
AR_B	34.94	34.87	1.05	1.08	14.6	15.2	276.5	285
NA_B	34.9	34.91	1.33	1.42	20.18	19.3	260.5	237
TA_B	34.86	34.87	1.56	1.64	23.81	23	242.4	217
SO_B	34.7	34.76	2.22	2.16	32.07	29.4	220.2	206
TIP_B	34.7	34.75	2.34	2.39	33.65	31.8	176.4	173
NP_B	34.69	34.71	2.51	2.52	36.02	33.4	155.9	144

sponding flow rates are consistent with tracer data and other observations (Sarmiento and Gruber, 2006).

The exchange fluxes between adjacent boxes reflect, both, opposing water flows across the box boundaries and eddy diffusive mixing (Table A3). The large vertical exchange flux between tropical surface and intermediate waters in the Indo-Pacific is thus supported by intense Ekman-driven upwelling and downwelling while wind-driven eddy diffusive mixing explains most of the vertical exchange between surface and intermediate water boxes in the North Atlantic, Southern Ocean, and North Pacific. The overall vertical water exchange across the 100 m water depth horizon (ca. 297 Sv, Table A3) is sufficiently high to ventilate the global thermocline and to support a global rate of new and export production in the order of 700–900 Tmol yr^{-1}. About 37 % of this vertical exchange flux occurs in the Southern Ocean (> 30° S). The global bidirectional water flux across the 2000 m water depth level is much lower (only 45 Sv, 44 % in the Southern Ocean) while the flux across the 4000 m line amounts to ca. 179 Sv with a 74 % contribution by the Southern Ocean. The box model's major internal boundary for vertical exchange is thus located at 2000 m water depth between the thermocline and the underlying deep ocean.

In box modelling, water fluxes (F_{Wab}) are multiplied by tracer concentrations (C_j) to calculate tracer fluxes (F_{Tab}) between adjacent boxes:

$$F_{Tab} = C_a \cdot F_{Wab}, \quad \text{(A1)}$$

where F_{Wab} and F_{Tab} are the water and tracer fluxes from box a to box b while C_a is the concentration of the considered tracer in box a. The back fluxes from box b to box a are defined correspondingly:

$$F_{Tba} = C_b \cdot F_{Wba}. \quad \text{(A2)}$$

Tracer fluxes arising from the water exchange fluxes listed in Table A3 (F_{Wex}) are thus proportional to the concentration difference between adjacent boxes:

$$F_{Tex} = (C_a - C_b) \cdot F_{Wex}. \quad \text{(A3)}$$

These fluxes can be regarded as diffusion-analogue mass transfer processes since their magnitude is proportional to concentration differences rather than concentrations. In contrast, the tracer fluxes arising from the net water fluxes in Table A3 are purely advective. Most box models apply unidirectional advective fluxes, only, and ignore diffusive bidirectional fluxes. Tracer distributions observed in the global ocean and simulated with general circulation models are, however, strongly affected by diffusive processes. With the

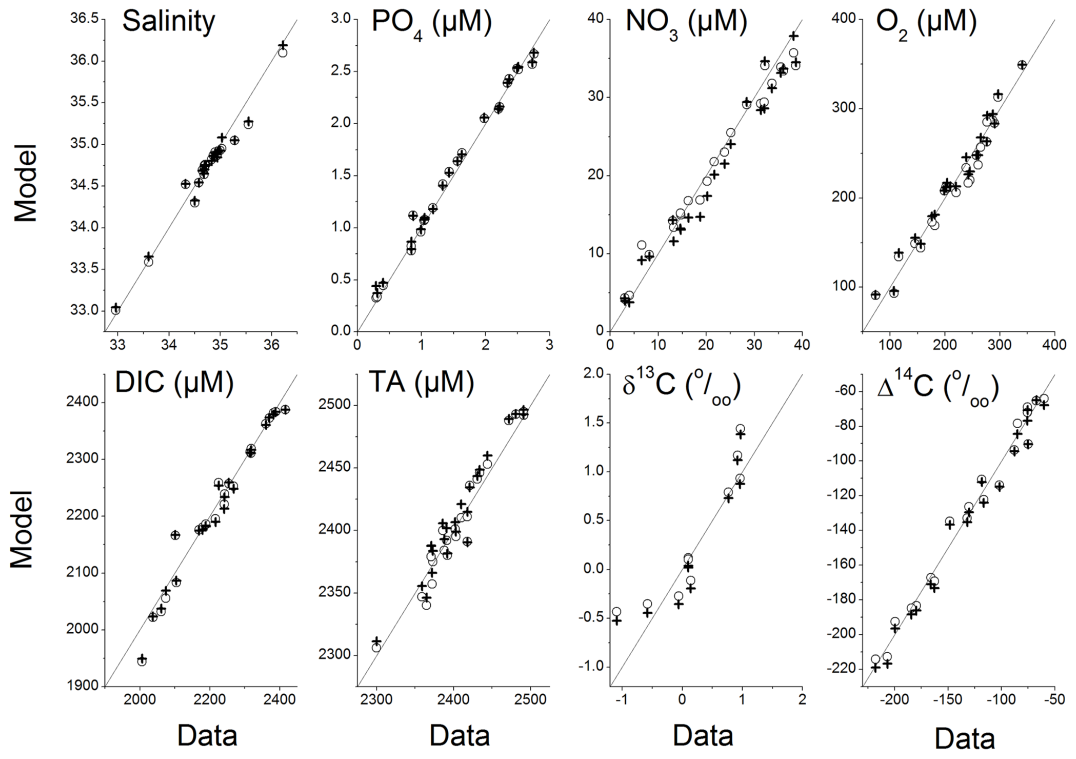

Figure A1. Tracer concentrations in ocean boxes: model vs. data. Open circles indicate concentrations applied as initial values at 130 ka (Tables A1 and A2). Crosses are concentrations obtained at the end of simulation STD at 0 ka after the completion of a full glacial cycle. Lines indicate the 1 : 1 relationship, e.g. the best fit to the data. δ^{13}C data at < 2000 m water depth are excluded from the model–data comparison since they are affected by anthropogenic CO_2.

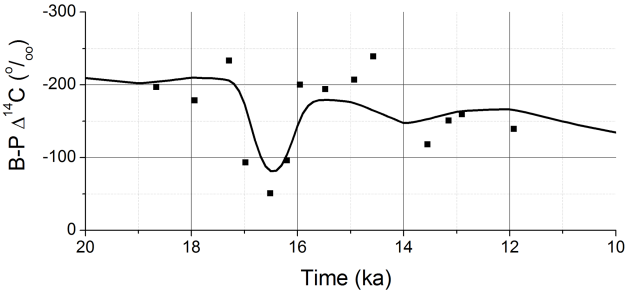

Figure A2. Deglacial benthic – pelagic radiocarbon record in the North Pacific: model (line) vs. data (squares). The Δ^{14}C-DIC difference between deep water and surface water boxes in the North Pacific is compared to data (Δ^{14}C difference between benthic and pelagic foraminifera, B-P Δ^{14}C) from core MD02-2489 taken at the Alaskan Margin at 3.6 km water depth (Rae et al., 2014). The vertical mixing across 100 and 2000 m water depth was enhanced by a factor of 10 at 16.5 ka (Fig. 4d) to reproduce the radiocarbon data.

inclusion of bidirectional fluxes in our box model set-up, we aim to better mimic this diffusive behaviour.

The low spatial resolution of box models is problematic and may induce significant errors. For the box model set-up presented in this paper, the largest errors are associated with the upward fluxes from the thermocline into the surface ocean. Tracer concentrations calculated for the intermediate water boxes represent mean values averaged over the depth range 100–2000 m where strong vertical gradients exist in the natural system. Due to these strong vertical gradients, the mean concentration values are not representative for the thermocline waters ascending across the 100 m water depth line. The standard box model approach where tracer fluxes are calculated applying the mean concentration in the source box (see equations above) was, thus, abandoned for these specific fluxes and tracer fluxes were calculated as

$$F_{\mathrm{TIS}} = C_{\mathrm{TH}} \cdot F_{\mathrm{WIS}}, \tag{A4}$$

where F_{TIS} is the tracer flux from the intermediate water box to the overlying surface water box, F_{WIS} is the corresponding water flux, and C_{TH} is the tracer concentration in the upwelling thermocline water calculated as

$$C_{\mathrm{TH}} = f_{\mathrm{I}} \cdot C_{\mathrm{I}} + (1 - f_{\mathrm{I}}) \cdot C_{\mathrm{S}}, \tag{A5}$$

where C_{I} is the concentration in the intermediate water box, C_{S} the concentration in the overlying surface water box, and f_{I} defines the fraction of C_{I} in the ascending two-component mixture. The weighing factor f_{I} was set to 0.5 for salinity,

Table A2. Dissolved inorganic carbon (DIC), total alkalinity (TA), δ^{13}C-DIC, and Δ^{14}C-DIC in model boxes (concentrations in µM, isotope data in ‰): model vs. data.

Box	DIC Data*	DIC Model	TA Data	TA Model	δ^{13}C Data^{+}	δ^{13}C Model	Δ^{14}C Data*	Δ^{14}C Model
AR_S	2101	2166	2372	2357	n. d.	2.11	n. d.	−68.26
NA_S	2074	2056	2410	2410	1.47	2.77	−75.6	−69.02
TA_S	2061	2032	2444	2453	1.64	2.77	−67.3	−65.35
SO_S	2104	2083	2365	2340	1.41	1.8	−85.1	−78.38
TIP_S	2006	1944	2359	2347	1.28	2.24	−60.1	−64.04
NP_S	2037	2022	2300	2306	1.3	2.27	−75.7	−72.01
AR_I	2169	2176	2373	2375	n. d.	1.79	n. d.	−78.03
NA_I	2179	2180	2391	2392	0.9	1.45	−75.	−90.32
TA_I	2225	2259	2386	2400	0.84	0.625	−101.8	−114
SO_I	2254	2257	2392	2380	0.72	−0.053	−130.4	−126.5
TIP_I	2317	2311	2418	2391	0.32	−0.653	−148.3	−134.7
NP_I	2370	2373	2421	2436	−0.23	−0.875	−179.7	−183.3
AR_D	2188	2185	2371	2379	n. d.	1.62	n. d.	−85.97
NA_D	2216	2195	2388	2384	0.97	1.44	−87.9	−93.75
TA_D	2242	2239	2402	2401	0.96	0.933	−116.6	−122.3
SO_D	2315	2314	2431	2441	0.1	0.119	−166.	−167.1
TIP_D	2382	2382	2481	2493	−0.06	−0.272	−199.6	−192.5
NP_D	2416	2388	2491	2492	−1.09	−0.432	−217.8	−214.2
AR_B	2188	2186	2371	2379	n. d.	1.6	n. d.	−86.2
NA_B	2241	2221	2403	2395	0.92	1.17	−118.4	−110.7
TA_B	2268	2253	2418	2411	0.77	0.792	−132.1	−132.9
SO_B	2318	2319	2434	2446	0.1	0.102	−162.7	−169.2
TIP_B	2360	2363	2472	2488	0.14	−0.111	−184.4	−184.7
NP_B	2388	2384	2491	2495	−0.58	−0.352	−206.8	−212.7

* Corrected for anthropogenic CO_2; $^{+}$ not corrected for anthropogenic CO_2.

DIC, and ^{13}C-DIC. A smaller value was applied for total alkalinity ($f_I = 0.3$) to mimic the deeper regeneration of this tracer while larger values were applied for other tracers featuring steeper thermocline gradients (DP and DN: $f_I = 0.55$; DO: $f_I = 0.9$; ^{14}C-DIC: 0.7).

A3 Salinity and surface temperatures

Salinity (Sal) was treated as an inert tracer. The mass balance equations for Sal in each of the 24 ocean boxes were thus simply defined as

$$\frac{\partial\,\mathrm{Vol}\cdot\mathrm{Sal}}{\partial\,t} = \sum F_{\text{Sal-in}} - \sum F_{\text{Sal-out}}, \tag{A6}$$

where $F_{\text{Sal-in}}$ are the salinity fluxes from the neighbouring boxes into the considered box while $F_{\text{Sal-out}}$ gives the corresponding fluxes from the considered box into the adjacent boxes. The volume of the considered box (Vol) was allowed to change over time to mimic the contraction of the ocean volume during glacial sea-level low-stands. Fluxes were calculated as products of water flux and salinity in the source box (Eqs. A1 and A2) with the exception of intermediate to surface water fluxes where thermocline concentrations were applied (Eqs. A4 and A5). Surface water boxes were subject to evaporation and precipitation and received river input from the continents. The freshwater fluxes listed in Table A3 represent the overall budget of evapotranspiration and river water input. Negative fluxes thus indicate that evaporation exceeds the sum of precipitation and river water input. Freshwater fluxes were varied in the initial steady-state simulations until the calculated salinity values were consistent with observations. These simulations showed, however, that unrealistically high freshwater fluxes were needed to reproduce the low salinity values observed in the Arctic Ocean surface water box. This problem arises since the standard box model procedure demands that water masses leaving the Arctic carry a chemical signature corresponding to the mean salinity value integrated over the entire Arctic surface ocean. Observations show, however, that Arctic surface waters sinking into the abyss are more salty than mean Arctic surface water. The standard model procedure was, hence, modified to consider this characteristic feature of deep water formation and to avoid unrealistically high freshwater fluxes to the Arctic surface ocean – that is an enhanced salinity (+ 0.9 PSU with respect to the mean salinity of Arctic surface water) was employed for the waters sinking into the underlying intermediate water box.

Table A3. Water fluxes (in Sv) derived from the NEMO model run and fluxes applied in the box model to reproduce observed tracer distributions (Tables A1 and A2).

Fluxes NEMO	NEMO Net	NEMO Exchange	Fluxes Box model	Box model Net	Box model Exchange
$NA_S \rightarrow AR_S$	1.1	2.64	$NA_S \rightarrow AR_S$	3.	1.74
$NA_S \rightarrow NA_I$	0.43	12.2	$NA_S \rightarrow NA_I$	9.93	42.2
$TA_S \rightarrow NA_S$	1.48	7.26	$TA_S \rightarrow NA_S$	12.83	0.36
$SO_S \rightarrow TA_S$	1.34	4.33	$SO_S \rightarrow TA_S$	12.94	0.43
$SO_S \rightarrow SO_I$	10.43	77.58	$SO_S \rightarrow SO_I$	3.93	106.58
$TIP_S \rightarrow SO_S$	8.16	12.42	$TIP_S \rightarrow SO_S$	15.94	12.42
$NP_S \rightarrow TIP_S$	0.43	10.93	$NP_S \rightarrow TIP_S$	0.31	2.93
$NP_S \rightarrow AR_S$	1.14	0.03	$NP_S \rightarrow AR_S$	1.14	0.03
$AR_S \rightarrow AR_I$	2.37	10.38	$AR_S \rightarrow AR_I$	4.37	45.38
$NA_I \rightarrow AR_I$	2.11	24.51	$NA_I \rightarrow AR_I$	2.11	14.51
$NA_I \rightarrow NA_D$	2.23	23.08	$NA_I \rightarrow NA_D$	8.23	0.08
$TA_I \rightarrow TA_S$	0.58	24.91	$TA_I \rightarrow TA_S$	0.58	0.41
$TA_I \rightarrow NA_I$	3.91	27.73	$TA_I \rightarrow NA_I$	0.41	17.73
$SO_I \rightarrow TA_I$	3.42	24.89	$TA_I \rightarrow SO_I$	0.08	4.87
$SO_I \rightarrow TIP_I$	1.29	88.37	$SO_I \rightarrow TIP_I$	13.79	73.37
$TIP_I \rightarrow TIP_S$	11.39	77.11	$TIP_I \rightarrow TIP_S$	16.39	77.11
$NP_I \rightarrow NP_S$	1.26	16.98	$NP_I \rightarrow NP_S$	1.26	3.98
$NP_I \rightarrow TIP_I$	2.	38.55	$NP_I \rightarrow TIP_I$	2.	3.55
$AR_I \rightarrow AR_D$	4.48	6.87	$AR_I \rightarrow AR_D$	6.48	6.87
$NA_D \rightarrow TA_D$	10.35	3.89	$NA_D \rightarrow TA_D$	15.35	1.19
$TA_D \rightarrow TA_I$	1.07	13.78	$TA_D \rightarrow TA_I$	1.07	8.78
$TA_D \rightarrow SO_D$	9.29	5.68	$TA_D \rightarrow SO_D$	15.29	1.68
$SO_I \rightarrow SO_D$	5.72	224.4	$SO_D \rightarrow SO_I$	9.78	10.12
$SO_D \rightarrow SO_B$	19.65	84.24	$SO_D \rightarrow SO_B$	17.65	114.24
$TIP_D \rightarrow TIP_I$	8.1	18.08	$TIP_D \rightarrow TIP_I$	0.6	3.08
$TIP_D \rightarrow SO_D$	4.64	12.54	$TIP_D \rightarrow SO_D$	12.14	2.54
$NP_D \rightarrow TIP_D$	5.71	10.96	$TIP_D \rightarrow NP_D$	1.29	0.67
$NP_D \rightarrow NP_I$	3.26	2.48	$NP_D \rightarrow NP_I$	3.26	1.48
$AR_D \rightarrow NA_D$	4.48	1.	$AR_D \rightarrow NA_D$	6.48	11.
$NA_B \rightarrow NA_D$	3.64	2.53	$NA_B \rightarrow NA_D$	0.64	2.53
$TA_B \rightarrow TA_D$	0.01	20.75	$TA_B \rightarrow TA_D$	1.01	20.75
$TA_B \rightarrow NA_B$	3.64	2.93	$TA_B \rightarrow NA_B$	0.64	0.43
$SO_B \rightarrow TA_B$	3.65	2.53	$SO_B \rightarrow TA_B$	1.65	2.53
$SO_B \rightarrow TIP_B$	16.	0.72	$SO_B \rightarrow TIP_B$	16.	15.72
$TIP_B \rightarrow TIP_D$	7.03	55.76	$TIP_B \rightarrow TIP_D$	14.03	35.76
$TIP_B \rightarrow NP_B$	8.97	8.65	$TIP_B \rightarrow NP_B$	1.97	0.65
$NP_B \rightarrow NP_D$	8.97	7.32	$NP_B \rightarrow NP_D$	1.97	7.32
$AR_B \rightarrow AR_D$	0	0.19	$AR_B \rightarrow AR_D$	0	1.19
$FRESH \rightarrow NA_S$	0.05		$FRESH \rightarrow NA_S$	0.10	
$FRESH \rightarrow TA_S$	−0.44		$FRESH \rightarrow TA_S$	−0.69	
$FRESH \rightarrow SO_S$	3.61		$FRESH \rightarrow SO_S$	0.93	
$FRESH \rightarrow TIP_S$	−3.66		$FRESH \rightarrow TIP_S$	−0.76	
$FRESH \rightarrow NP_S$	0.31		$FRESH \rightarrow NP_S$	0.19	
$FRESH \rightarrow AR_S$	0.13		$FRESH \rightarrow AR_S$	0.23	

Over a glacial cycle, surface temperatures are regulated by changes in, both, albedo and the partial pressure of greenhouse gases. In the model it was assumed that 50 % of the temperature change is proportional to the prescribed sea-level change (e.g. continental ice sheet formation and albedo change) while the remaining 50 % is proportional to the logarithm of atmospheric pCO_2 calculated as prognostic model variable. The global mean atmospheric surface temperature was assumed to fall by 3 °C during the glacial while the average SST was allowed to drop by ca. 2 °C (Schmittner et al., 2011). The SST drop was assumed to be twice as high as the global mean at high latitudes and only half as high in the

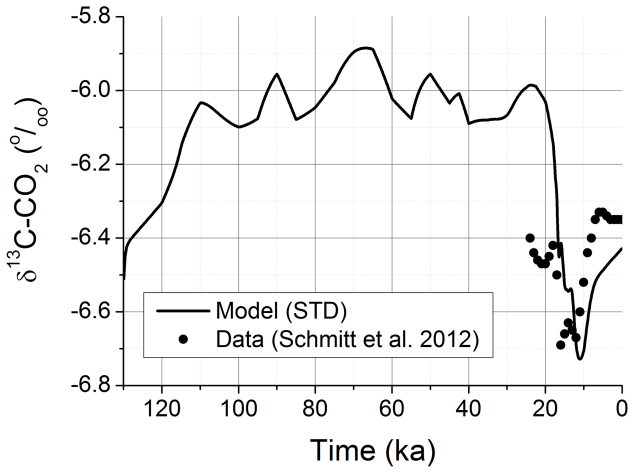

Figure A3. Stable carbon isotopic composition of atmospheric CO_2. Model results vs. ice-core data (Schmitt et al., 2012). The model results were obtained in the standard simulation STD without any tuning of the ^{13}C-CO_2 fluxes across the seawater–atmosphere interface.

low-latitude surface water boxes. Temperatures in intermediate and deep waters were maintained at their modern values, for simplicity.

A4 Phosphorus

The model includes a comprehensive phosphorus cycle. Rivers transport dissolved phosphorus (DP) into the ocean where it is taken up by phytoplankton, gets exported, degraded, buried in marine sediments, and removed via hydrothermal activity (Wallmann, 2014). Export production (F_{EPOP}) of particulate organic P (POP) from the individual surface water boxes across 100 m water depth was calculated applying Liebig's law:

$$F_{EPOP} = k_{EXP} \cdot \mathrm{Min}\left[DP_S \cdot \frac{DP_S}{DP_S + K_{DP}}, \frac{DN_S}{r_{NP}} \cdot \frac{DN_S}{DN_S + r_{NP} \cdot K_{DP}}\right] \cdot Vol_S. \quad \text{(A7)}$$

POP export was thus limited either by dissolved reactive nitrogen (DN) or DP where K_{DP} is a Monod constant ($K_{DP} = 0.01$ µM), r_{NP} is the atomic N to P ratio in exported particulate organic matter ($r_{NP} = 17$, Körtzinger et al., 2001), Vol_S is the volume of the considered surface water box, and k_{EXP} is a site-specific kinetic constant defined by fitting the model to DP concentrations observed in the modern surface ocean (Table A4). Most of the exported POP was degraded in the water column while a small but significant fraction was permanently buried in marine sediments (Appendix B). POP degradation in the water column (including the bioturbated surface layer of marine sediments) was distributed between intermediate (93 %), deep (6 %), and bottom water boxes (1 %). Export and degradation of particulate organic carbon (POC) and nitrogen (PON) and oxygen respiration were derived from the corresponding POP turnover applying constant Redfield ratios (PON/POP = 17, POC/PON = 123/17, O_2/POC = 1.34, Körtzinger et al., 2001).

A5 Nitrogen

Nitrogen cycling was simulated considering export, degradation, and burial of PON, nitrogen fixation, benthic and pelagic denitrification, and riverine fluxes of dissolved reactive nitrogen (DN). Nitrogen fixation in surface water boxes (F_{NF}) was calculated as

$$F_{NF} = k_{NF} \cdot DP_S \cdot \frac{DP_S}{DP_S + K_{DP}} \cdot \frac{r_{NP}}{r_{DNDPS}} \cdot Vol_S. \quad \text{(A8)}$$

It was controlled by the ambient DP concentration and modulated by the DN / DP ratio in surface water (r_{DNDPS}) such that nitrogen fixation decreased when r_{DNDPS} exceeded the N / P ratio in exported biomass (r_{NP}) and vice versa. The biomass of nitrogen-fixing organisms was completely degraded in the surface ocean boxes and the organic nitrogen compounds were transformed into DN. Nitrogen fixation thus enhanced the DN pool in the surface ocean but did not contribute to export production. The kinetic constant for nitrogen fixation (k_{NF}) was determined by fitting the model to the nitrate concentrations observed in the modern surface ocean (Tables A1 and A4).

Denitrification in the water column was limited to the intermediate water box of the Tropical Indo-Pacific where the major oxygen minimum zones (OMZs) are located. It proceeded at a constant rate of 5 Tmol yr^{-1} (Deutsch et al., 2001). No attempt was made to simulate the temporal evolution of water column denitrification since the box model did not resolve the dynamics and spatial extent of OMZs. Benthic denitrification was calculated as a function of bottom water chemistry (nitrate and oxygen) and the rain rate of particulate organic carbon (POC) to the seafloor (Appendix B) using an empirical transfer function (Bohlen et al., 2012).

A6 Oxygen

Oxygen was produced in the surface ocean via export production and consumed in the ocean's interior by degradation of particulate organic matter. The oxygen exchange between surface ocean and atmosphere was calculated as

$$F_{DO} = k_W \cdot A_{SUR} \cdot \left(DO_S - DO_{SEQ}\right), \quad \text{(A9)}$$

where k_W is piston velocity, A_{SUR} is the ice-free surface area of the considered box (Köhler et al., 2005), DO_S is the concentration of DO in the considered surface water box, while DO_{SEQ} is the temperature-dependent equilibrium concentration of DO in surface water (García and Gordon, 1992). The piston velocity was determined for each surface water box by fitting the model to the observed $\Delta^{14}C$ values (Tables A2

Table A4. Biogeochemical parameter values determined by fitting the model to observations.

Parameter	Symbol	Units	AR	NA	TA	SO	TIP	NP
Kinetic constant for export production	k_{EXP}	yr^{-1}	0.05	1.5	0.4	0.15	1.1	0.12
Kinetic constant for nitrogen fixation	k_{NF}	yr^{-1}	0.0	3.0	1.0	0.2	1.0	0.5
PIC / POC export ratio	r_{PICPOC}		0.01	0.08	0.20	0.01	0.15	0.07
Piston velocity	k_{SA}	$cm\,yr^{-1}$	0.4	0.1	0.12	0.12	0.24	0.1

Table A5. Difference in δ^{13}C-DIC between LGM (21 kyr BP) and Holocene (5 kyr BP) as derived from data (Oliver et al., 2010; Sarnthein et al., 1994) and calculated in the standard model run.

Box	Data	Model
NA_I	$+0.04 \pm 0.28$	$+0.01$
NA_D	-0.55 ± 0.16	-0.60
NA_B	-0.70 ± 0.13	-0.70
TA_I	$+0.15 \pm 0.20$	$+0.22$
TA_D	-0.55 ± 0.24	-0.66
TA_B	-0.78 ± 0.21	-0.73
SO_D	-0.44 ± 0.26	-0.52
TIP_D	-0.44 ± 0.20	-0.36

and A4). The deep ocean is ventilated by cold and oxygen-enriched surface waters sinking into the ocean's interior at high latitudes with a temperature of ca. −1.5 °C. To mimic this process in the box model, the oxygen concentration in downward-flowing water masses was calculated by applying a temperature of −1.5 °C rather than the significantly higher mean SSTs of North Atlantic and Southern Ocean surface waters.

A7 Carbon

POC burial depended on export production and depositional area while neritic carbonate burial was proportional to the shelf area at 0–50 m water depths (Appendix B). Export of pelagic PIC (particulate inorganic carbon) was calculated from POC export production and the PIC / POC export ratios which were derived by fitting the TA values in the surface ocean to observations (Tables A2 and A4). Exported PIC dissolved in intermediate water boxes until the PIC / POC export ratio at 2000 m water depth reached a value of unity as observed in sediment trap studies (Berelson et al., 2007; Honjo et al., 2008). Carbonate compensation was implemented at > 2000 m water depth where PIC dissolution was controlled by the carbonate ion concentrations calculated from TA and DIC values in deep and bottom water boxes (Wallmann, 2014). The remaining PIC was buried in pelagic sediments. The TA mass balance equations considered alkalinity production via denitrification and PON export production and alkalinity consumption via nitrogen fixation and PON degradation. The CO_2 gas flux from the surface ocean into the atmosphere across the seawater/atmosphere boundary layer (F_{CO_2}) was calculated as (Sarmiento and Gruber, 2006)

$$F_{CO_2} = k_W \cdot A_{SUR} \cdot \left(CO_{2S} - CO_{2SEQ}\right), \quad \text{(A10)}$$

where CO_{2S} is the concentration of CO_2 in the considered surface water box (as calculated from ambient DIC and TA), while CO_{2SEQ} is the equilibrium concentration of CO_2 in surface water (as calculated from atmospheric pCO_2). The thermodynamic equations included in the box model considered the effects of SST and salinity on CO_{2SEQ} and CO_{2S} (Zeebe and Wolf-Gladrow, 2001). Constant rates were applied for on-shore volcanic and metamorphic degassing, degassing at mid-ocean ridges, alteration of oceanic crust, and silicate weathering (Wallmann, 2014). The rate of silicate weathering was set to a constant value since the weathering of exposed shelf sediments was assumed to compensate for the glacial decrease in silicate weathering in the continental hinterland (Munhoven, 2002). The rate of carbonate weathering was assumed to depend on surface temperature, run-off, and the size of the exposed shelf area (Wallmann, 2014). Riverine POC fluxes are ignored in the model. However, POC weathering is considered. It has two components: (i) weathering of POC in exposed shelf sediments and (ii) weathering of fossil POC in continental hinterland (Wallmann, 2014). Both components produce atmospheric CO_2 depleted in ^{13}C and ^{14}C.

A8 Carbon isotopes

The model includes ^{13}C-DIC and ^{14}C-DIC as tracers in addition to total DIC. Isotope ratios as well as δ^{13}C and Δ^{14}C values of DIC were calculated from ^{13}C-DIC/DIC and ^{14}C-DIC/DIC mole fractions. The gas exchange of ^{13}C-CO_2 across the seawater/atmosphere boundary layer (F_{13CO2}) was

calculated as (Schmittner et al., 2013; Zhang et al., 1995)

$$F_{13CO2} = k_W \cdot A_{SUR} \cdot \alpha_{aq-g} \cdot \alpha_k \cdot \left(\frac{R_{13DIC}}{\alpha_{DIC-g}} \cdot CO_{2S} - R_{13CO2A} \cdot CO_{2SEQ} \right), \quad (A11)$$

where α_{aq-g} is the equilibrium fractionation factor for CO_2 gas exchange between seawater and air, α_k is the corresponding kinetic fractionation factor, α_{DIC-g} is the equilibrium fractionation factor defining the ^{13}C fractionation between DIC and gaseous CO_2, R_{13DIC} is the ^{13}C / ^{12}C ratio in DIC, and R_{13CO2A} is the ^{13}C / ^{12}C ratio in atmospheric CO_2. The isotopic composition of DIC species (CO_2, HCO_3^-, CO_3^{2-}) was calculated using equilibrium fractionation factors given in Zeebe and Wolf-Gladrow (2001). These values were applied to calculate the isotopic composition of exported POC and neritic and pelagic carbonates applying isotopic fractionation factors according to Ridgewell (2001) and Romanek et al. (1992), respectively.

Figure A3 shows the atmospheric $\delta^{13}C$-CO_2 record as calculated in our standard simulation. According to this simulation and our previous studies (Sarnthein et al., 2013), the strong negative $\delta^{13}C$-excursion observed in the ice-core record was largely caused by deglacial upwelling pulses in the Southern Ocean, though the amplitude of the simulated $\delta^{13}C$-CO_2 decline is much larger than that observed in the data set (Schmitt et al., 2012). The trends of our results and the empiric data are similar. The different extent of shift of the two records is probably related to the poor representation of the ^{13}C-DIC turnover in the Southern Ocean in our coarse-resolution model. We were not able to reproduce more closely the observed $\delta^{13}C$-DIC distribution in our model calibration even though a good fit was attained for all other tracers (salinity, DIC, ^{14}C-DIC, alkalinity, phosphate, nitrate, oxygen, Fig. A1). Hence, we do not conclude that this deviation for $\delta^{13}C$-CO_2 implies erroneous model results for all remaining model variables. It rather reflects a specific weakness in the model set-up with respect to the simulation of $\delta^{13}C$-DIC in the Southern Ocean. Our model predicts a negative value for intermediate waters in the modern Southern Ocean ($\delta^{13}C$-DIC $= -0.05$ ‰) while observations yield a positive value of $+0.72$ ‰ for this ocean box (SO_I in Table A2). Due to this deviation the vertical gradient in the model exceeds the observed $\delta^{13}C$ gradient between surface and intermediate waters by more than a factor of two. The glacial rise and deglacial drop in $\delta^{13}C$-CO_2 are amplified by this model artefact. The deglacial intermediate water, overly depleted in ^{13}C, upwells into the surface ocean where it induces a far too strong atmospheric $\delta^{13}C$-CO_2 decline. Since the biased vertical $\delta^{13}C$-DIC gradient in the Southern Ocean impedes a meaningful simulation of atmospheric $\delta^{13}C$-CO_2, we tuned the ^{13}C-CO_2 fluxes between the surface ocean and the atmosphere such that the resulting atmospheric $\delta^{13}C$-CO_2 values were consistent with the ice-core record. By this way we effectively employed the ice-core data to force the $\delta^{13}C$-DIC model (Fig. 4f). The $\delta^{13}C$ values of intermediate, deep and bottom water boxes employed to derive the glacial circulation field (Table A5) were not significantly affected by this tuning since the inventory of ^{13}C residing in the global ocean exceeds the atmospheric inventory by almost two orders of magnitude.

The ^{14}C / ^{12}C fractionation between DIC, CO_2, POC, and $CaCO_3$ was calculated using the squared ^{13}C equilibrium fractionation factors since the mass difference between ^{14}C and ^{12}C exceeds the ^{13}C–^{12}C difference by a factor of 2. The gas exchange of ^{14}C-CO_2 across the seawater/atmosphere boundary layer (F_{14CO2}) was thus calculated as

$$F_{14CO2} = k_W \cdot A_{SUR} \cdot \alpha_{aq-g}^2 \cdot \alpha_k \cdot \left(\frac{R_{14DIC}}{\alpha_{DIC-g}^2} \cdot CO_{2S} - R_{14CO2A} \cdot CO_{2SEQ} \right), \quad (A12)$$

where R_{14DIC} is the ^{14}C / ^{12}C ratio in DIC of the considered surface water box and R_{14CO2A} the ^{14}C / ^{12}C ratio in atmospheric CO_2. Moreover, ^{14}C-DIC was subject to radioactive decay with a decay constant of $\lambda = \frac{1}{8267}$ yr^{-1}.

$\Delta^{14}C$-DIC values were calculated as

$$\Delta^{14}C - DIC = \left(\frac{f_N \cdot \Phi_{14DIC}}{\Phi_{abs}} - 1 \right) \cdot 1000, \quad (A13)$$

where Φ_{14DIC} is the ^{14}C mole fraction (Φ_{14DIC} = ^{14}C-DIC/DIC), Φ_{abs} is the ^{14}C mole fraction of the standard (1.175×10^{-12}; Mook and Plicht, 1999) pre-human atmosphere with a $\delta^{13}C$ value of -25 ‰, f_N is the normalization factor defined as

$$f_N = \left(\frac{0.975}{\left(1 + \frac{\delta^{13}C}{1000}\right)} \right)^2, \quad (A14)$$

and $\delta^{13}C$ is the $\delta^{13}C$ value of DIC in the considered box in ‰ PDB. The isotopic fractionation experienced by the considered DIC pool was thus taken into account in the calculation of marine $\Delta^{14}C$-DIC values by applying the $\delta^{13}C$-DIC calculated for the considered ocean box (Stuiver and Polach, 1977).

The time-dependent radiocarbon production rate in the atmosphere (R_{14}) was calculated by applying

$$R_{14} = k_{14}(\Delta^{14}C - CO_2(data) - \Delta^{14}C - CO_2(model)), \quad (A15)$$

where k_{14} is a constant ($\geq 10^5$ mmol yr^{-1} ‰), $\Delta^{14}C$-CO_2 (model) is the atmospheric value calculated for each time step of the model, and $\Delta^{14}C$-CO_2 (data) is the data trend reconstructed from the geological record (Reimer et al., 2013). R_{14} thus increased when $\Delta^{14}C$-CO_2 (model) was smaller than $\Delta^{14}C$-CO_2 (data) and vice versa. With this approach, the production rate was varied such that the model always

complied with the atmospheric ^{14}C record. The atmospheric radiocarbon model considered production and the decay of radiocarbon in the atmosphere as well as exchange processes with the continents and the surface ocean (Eq. A12). The major output of the atmospheric ^{14}C model was the time-dependent ^{14}C production rate (Eq. A15).

Appendix B: Impact of sea-level change on benthic processes at continental margins

B1 Particulate organic carbon (POC) turnover

The overwhelming portion of POC produced in the euphotic zone is degraded in the water column before it can reach the seabed. Hence, in the open ocean, only ca. 1 % of the primary production is deposited at the deep-sea floor (Suess, 1980; Jahnke, 1996; Seiter et al., 2005; Dunne et al., 2007). However, the fraction reaching the seabed increases drastically at continental margins where shallow water depths limit the transit time of POC sinking through the water column. Global models and observations thus indicate that ca. 30 % of ambient primary production reaches the shallow seafloor at 0–50 m water depth (Dunne et al., 2007). Due to this effect and the high productivity of continental margins, the margin seabed located at < 2 km water depths receives ca. 85 ± 15 % of the global POC rain rate (Dunne et al., 2007; Burdige, 2007) even though only 16 % of the global seabed is located at < 2 km water depth (Eakins and Sharman, 2012). Continental margins are even more dominant in terms of POC burial because burial is promoted by the deposition of riverine particles (Berner, 1982, 2004) accumulating mostly on the continental shelf during interglacial sea-level high-stands (Burwicz et al., 2011). Thus, 90 ± 10 % of the global POC burial takes place at < 2 km water depth (Dunne et al., 2007; Burdige, 2007; Wallmann et al., 2012).

POC rain and burial rates at continental margins declined during glacial sea-level low-stands since the oceans retreated into steeper terrains. During the LGM when the sea-level was 120 m lower than today, the shelf seafloor area at 0–100 m contracted by 73 % while the outer shelf and upper slope area located at 100–2000 m water depth was reduced by 13 % (Eakins and Sharman, 2012) neglecting isostatic adjustment. Considering the high rain rates at shallow water depths (Dunne et al., 2007), the glacial margin contraction diminished the global POC rain rate by possibly up to 50 %. The burial rate of marine POC may have been reduced by a similar proportion since POC burial is ultimately limited by the amount of POC reaching the seabed. However, there are a number of additional factors that affect the rate of POC burial. These include bulk sedimentation rate (Berner, 1982), surface area of sediment particles (Mayer et al., 2004), oxygen exposure time (Hartnett et al., 1998), and the resuspension and down-slope transport of shelf POC promoting POC burial at the upper slope (Walsh et al., 1981; Dale et al., 2015). These secondary processes control the burial efficiency of POC, that is the ratio between POC burial and POC rain rate.

POC burial efficiency is to a large degree controlled by sedimentation processes on the shelf that are strongly affected by sea-level change. At high sea-level most of the riverine particle load is deposited on the shelf (Burwicz et al., 2011) while low sea-level stands promote down-slope transport (Hay and Southam, 1977). Hence, data on Quaternary shelf and deep-sea fan sedimentation clearly show that the riverine particle flux was discharged over the shelf edge onto deep-sea fans and abyssal plains by turbidity currents over most of the glacial period (Hay and Southam, 1977; Hay, 1994; Schlünz et al., 1999). The corresponding increase in sedimentation rate probably led to a rise in burial efficiency and POC burial at > 2 km water depths (Burwicz et al., 2011; Wallmann, 2014). The efficiency of POC burial at the continental rise and deep-sea floor may have been further amplified by the glacial decline in dissolved oxygen concentrations in the deep ocean (Jaccard and Galbraith, 2012) favouring the preservation of POC in marine sediments (Hartnett et al., 1998; Dale et al., 2015). It is difficult to validate glacial changes in burial efficiency at < 2 km water depths. Here, POC preservation was possibly reduced by the intense ventilation of the glacial thermocline (Jaccard and Galbraith, 2012) while preservation might have been enhanced if sedimentation rates on the outer shelf and upper slope were significantly elevated by the glacial loss of inner shelf regions. Considering the available evidence it can be concluded that the glacial marine regression induced a strong decline in POC burial on the continental shelf while POC burial was enhanced at the continental rise and deep-sea floor. The overall effect was an increase in water column degradation and decline in marine POC burial since the focus of POC burial was shifted to > 2 km water depth where rain and burial rates are limited by the almost complete degradation of marine POC in the water column.

B2 Nutrient turnover

Continental margins are also major sinks for nitrate and phosphate since > 50 % of the global benthic denitrification and burial of marine phosphorus occur in sediments deposited at < 2 km water depth (Bohlen et al., 2012; Archer et al., 2002; Froelich et al., 1982; Baturin and Savenko, 1997; Wallmann, 2010; Middelburg et al., 1996). These fluxes are driven by the rain of marine POM to the seabed which is focused on shallow water environments (Dunne et al., 2007). The strong decrease in shallow seafloor area during glacial marine regressions thus induced a decline in nitrate and phosphate removal contributing to the expansion of the nutrient inventory in the glacial ocean (Broecker, 1982b; Deutsch et al., 2004; Eugster et al., 2013; Wallmann, 2014). A negative feedback was probably established whereby the expansion of the nutrient inventory induced a rise in export production and rain rate to the seabed which in turn promoted the burial of POC and removal of nutrients from the ocean. The glacial decline in POC burial and the glacial rise in the standing stocks of macronutrients may have been mitigated by this negative feedback mechanism (Middelburg et al., 1996).

Phosphate cycling in marine sediments is affected by oxygen conditions in ambient bottom waters and sediments (Krom and Berner, 1981; Van Cappellen and Ingall, 1994;

Table B1. Parameter values applied in the simulation of margin processes.

Parameter	Symbol	Value	Source
Modern seafloor area at 0–50 m	A_{NM}	13.54×10^6 km^2	Eakins and Sharman (2012)
Modern seafloor area at 0–100 m	A_{SM}	20.34×10^6 km^2	Eakins and Sharman (2012)
Modern seafloor area at 100–2000 m	A_{IM}	38.29×10^6 km^2	Eakins and Sharman (2012)
Modern rate of neritic carbonate burial	F_{BPICSM}	10 Tmol yr^{-1}	Kleypas (1997)
Modern rate of marine POC burial at 0–100 m	F_{BPOCSM}	5 Tmol yr^{-1}	Wallmann et al. (2012)
Modern rate of marine POC burial at 100–2000 m	F_{BPOCIM}	5 Tmol yr^{-1}	Wallmann et al. (2012)
Modern rate of marine POC burial at 2000–4000 m	F_{BPOCDM}	1.3 Tmol yr^{-1}	Wallmann et al. (2012)
Modern rate of marine POC burial at > 4000 m	F_{BPOCBM}	0.2 Tmol yr^{-1}	Wallmann et al. (2012)
Modern POC export production	F_{EPOCM}	809 Tmol yr^{-1}	Sarmiento and Gruber (2006)
Modern rate of marine P burial at 0–100 m	F_{BPSM}	0.05 Tmol yr^{-1}	Wallmann (2010)
Modern rate of marine P burial at 100–2000 m	F_{BPIM}	0.05 Tmol yr^{-1}	Wallmann (2010)
Modern rate of marine P burial at 2000–4000 m	F_{BPDM}	0.06 Tmol yr^{-1}	Wallmann (2010)
Modern rate of marine P burial at > 4000 m	F_{BPBM}	0.02 Tmol yr^{-1}	Wallmann (2010)
Monod constant for P burial	k_P	20 µM	Wallmann (2010)
Burial efficiency of marine POC at 0–100 m	BE_S	0.05	This work
Burial efficiency of marine POC at 100–2000 m	BE_I	0.2	This work
Burial efficiency of marine POC at 2000– 4000 m	BE_D	0.1	This work
Burial efficiency of marine POC at > 4000 m	BE_B	0.02	This work
Maximum POC to P ratio in marine sediments	r_{CPM}	400	Anderson et al. (2001)

Table B2. Flux parametrizations applied in the simulation of margin processes.

Process	Equation*
Neritic carbonate burial	$F_{BPICS} = F_{BPICSM} \cdot \frac{A_N}{A_{NM}}$
POC burial at 0–100 m	$F_{BPOCS} = F_{BPOCSM} \cdot \frac{F_{EPOC}}{F_{EPOCM}} \cdot \frac{A_S}{A_{SM}}$
POC burial at 100–2000 m	$F_{BPOCI} = F_{BPOCIM} \cdot \frac{F_{EPOC}}{F_{EPOCM}} \cdot \frac{A_I}{A_{IM}}$
POC burial at 2000–4000 m	$F_{BPOCD} = F_{BPOCDM} \cdot \frac{F_{EPOC}}{F_{EPOCM}} \cdot \frac{A_{SM}+A_{IM}}{A_S+A_I}$
POC burial at > 4000 m	$F_{BPOCB} = F_{BPOCBM} \cdot \frac{F_{EPOC}}{F_{EPOCM}} \cdot \frac{A_{SM}+A_{IM}}{A_S+A_I}$
P burial at 0–100 m	$F_{BPS} = \mathrm{Max}\left[F_{BPSM} \cdot \frac{F_{EPOC}}{F_{EPOCM}} \cdot \frac{A_S}{A_{SM}} \cdot \frac{DO_S}{DO_S+k_P} \cdot \frac{DO_{SM}+k_P}{DO_{SM}}, \frac{F_{BPOCS}}{r_{CPM}}\right]$
P burial at 100–2000 m	$F_{BPI} = \mathrm{Max}\left[F_{BPIM} \cdot \frac{F_{EPOC}}{F_{EPOCM}} \cdot \frac{A_I}{A_{IM}} \cdot \frac{DO_I}{DO_I+k_P} \cdot \frac{DO_{IM}+k_P}{DO_{IM}}, \frac{F_{BPOCI}}{r_{CPM}}\right]$
P burial at 2000–4000 m	$F_{BPD} = \mathrm{Max}\left[F_{BPDM} \cdot \frac{F_{EPOC}}{F_{EPOCM}} \cdot \frac{DO_D}{DO_D+k_P} \cdot \frac{DO_{DM}+k_P}{DO_{DM}}, \frac{F_{BPOCD}}{r_{CPM}}\right]$
P burial at > 4000 m	$F_{BPB} = \mathrm{Max}\left[F_{BPBM} \cdot \frac{F_{EPOC}}{F_{EPOCM}} \cdot \frac{DO_B}{DO_B+k_P} \cdot \frac{DO_{BM}+k_P}{DO_{BM}}, \frac{F_{BPOCB}}{r_{CPM}}\right]$
Benthic denitrification with i = (S, I, D, B)	$F_{BDENi} = \frac{F_{BPOCi}}{BE_i} \cdot (0.06 + 0.19 \cdot 0.99^{(DO_i - DN_i)})$

* Subscripts indicate modern values (M) and the following environments: shelf (S, 0–100 m water depth), outer shelf and slope (I, 100–2000 m), continental rise and deep-sea floor (D, 2000–4000 m), deep-sea floor and abyssal plain (B, > 4000 m). The equations define global fluxes. These were distributed among the ocean basins according to their export production and the seafloor areas of individual boxes.

Wallmann, 2003). Phosphate is released from sediments under suboxic and anoxic conditions due to the reduction of iron and manganese oxides and the preferential degradation of P-bearing organic matter (POP). However, a large fraction of the released phosphate is precipitated and retained in the sediment as authigenic carbonate fluorapatite (CFA). Hence, OMZ sediments are depleted in Fe / Mn-bound P, enriched in CFA and characterized by high POC / POP ratios exceeding the Redfield ratio by a factor of 2–8 (Schenau and De Lange, 2001; Lomnitz et al., 2015). Ratios between POC and reactive P (P_{reac}: sum of POP, CFA, and Fe / Mn-bound P) amount to $POC/P_{reac} = 100–300$ in OMZ sediments and 20–70 in continental margin sediments underlying oxygenated bottom waters (Schenau and De Lange, 2001; Noffke et al., 2012). Hence, the burial efficiency of reactive P and total P is reduced under low-oxygen conditions (Ingall and Jahnke, 1994; Schenau and De Lange, 2001) whereas POC is more efficiently buried in OMZ sediments covered by oxygen-depleted bottom waters (Dale et al., 2015).

B3 Equations and parameter values employed to simulate carbon and nutrient turnover

The parametrization of margin processes applied in the model is summarized in Tables B1 and B2. A very simple approach was chosen to calculate the burial of neritic carbonates. It was assumed that the burial rate is proportional to the seafloor area at 0–50 m water depth (A_{NM}) which is controlled by sea-level change, only (see Fig. 3). Burial of marine POC and phosphorus (P) at continental margins was assumed to be proportional to POC export production (F_{EPOC}) and the depositional areas at 0–100 m (A_S) and 100–2000 m (A_I) that were controlled by sea-level change (Fig. 3). The decline in seafloor area at 0–2000 m water depths was applied to parametrize the rise in POC burial at the deep-sea floor induced by the glacial marine regression. We thus effectively assumed that the burial efficiency of POC remained constant at < 2 km water depth but increased at > 2km during glacial sea-level low-stands.

Phosphorus considered in the model refers to the sum of organic and reactive inorganic P phases (CFA and Fe / Mn-bound P). The latter fractions contribute strongly to P burial since most of the marine particulate P deposited at the seafloor is degraded and transformed into inorganic authigenic phases during early diagenesis (Ruttenberg and Berner, 1993). P burial decreases when the dissolved oxygen content of ambient bottom waters (DO) falls below a threshold value of about 20 µM (Wallmann, 2010). This effect was taken into account by introducing corresponding Monod terms in the P burial flux definitions (Table B2). Moreover, the model formulation ensured that the molar POC / P_{reac} burial ratio did not exceed the maximum value of about 400 observed in Quaternary sediments (Anderson et al., 2001).

Benthic denitrification was calculated from the POC rain rate and ambient dissolved oxygen and nitrate concentrations (DN) applying an empirical transfer function calibrated by in-situ benthic flux data (Bohlen et al., 2012). The rain rates needed for this function were derived from POC burial rates using the corresponding burial efficiencies. Marine PON burial was calculated from POC burial applying a molar PON / POC ratio of 17/123 (Körtzinger et al., 2001).

In contrast to previous sediment models (Heinze et al., 1999; Gehlen et al., 2006), our model does not resolve transport processes and reactions within surface sediments. We prefer to employ observational data on POC and P burial and empirical transfer functions to constrain benthic turnover rates (Bohlen et al., 2012; Wallmann, 2010) because most depth-resolving transport–reaction models yield results that are not yet consistent with key data such as benthic oxygen and nitrate fluxes and POC burial rates (Stolpovsky et al., 2015).

The applied parameter values were constrained by field data from the modern ocean (Table B1). The available POC and P burial data suggest that burial is rather evenly distributed between 0–100 and 100–2000 m water depths (Table B1) whereas POM rain rates at 0–100 m clearly exceed the corresponding rates at 100–2000 m (Dunne et al., 2007). This difference is caused by bottom currents transporting marine POM from the inner shelf towards outer shelf and upper slope environments (Walsh et al., 1981). Note that the POC burial rates applied in our model (Table B1) are conservative – that is, lower than most previous estimates (Burdige, 2007; Dunne et al., 2007). The burial efficiency applied in the model is low at shallow water depth since winnowing by bottom currents affects large parts of the shallow seafloor such that about 70 % of the modern shelf sediments are non-accumulating, relict sands with very low POC contents (Burdige, 2007). POM exported laterally from these shallow areas provides POM for slope deposits (Walsh et al., 1981). The highest burial efficiency is applied at 100–2000 m water depth where the deposition of fine-grained riverine particles and low oxygen values in ambient bottom waters favour the preservation of marine POC. Parameter values and fluxes listed in Tables B1 and B2 refer to global fluxes. These fluxes were distributed among the six ocean basins defined in the box model considering the respective seafloor areas and export productions. Neritic carbonate burial was distributed between the Tropical Indo-Pacific and Atlantic (Kleypas, 1997).

Our model predicts that the global burial rates of marine POC and P would decline to 7.9 and 0.14 Tmol yr^{-1} during the LGM, respectively, if export production and oxygen concentrations were maintained at their modern value. The export production was, however, promoted by the decline in P burial such that the best-fit simulation STD produced LGM burial rates of 9.6 and 0.165 Tmol yr^{-1} compared to modern global rates of 11.5 and 0.18 Tmol yr^{-1}, respectively (see Table B1). Our standard model run suggests that the shelf (0–100 m water depths) trapped a total of 4650 Gt POC over the last glacial cycle (130–0 ka) while 7870 Gt POC accumulated on the continental slope (100–2000 m water depth). Shelf weathering released a total of 1940 GtC over the last 130 ka in simulation STD – namely, less than 50 % of the POC accumulating on the shelf over the last glacial cycle. According to the model, the glacial marine regression affected the chemical and isotopic composition of seawater and the CO_2 content of the atmosphere via a chain of interconnected processes: ocean margins retreated into steeper terrain and shelf areas were exposed by the marine regression; the burial of phosphorus and neritic carbonate and benthic denitrification declined due to the steepening of ocean margins; carbonate, POC, and P weathering rates increased due to the exposure of shelf sediments; atmospheric CO_2 was consumed and converted into dissolved alkalinity by enhanced carbonate weathering while isotopically depleted CO_2 was released into the atmosphere by POC weathering; standing stocks of dissolved nutrients and alkalinity in the ocean expanded due to the decrease in burial and denitrification and the increase in weathering; export production rose due to the increase in the dissolved nutrient stocks and CO_2 was transferred from

the atmosphere into the ocean interior by the intensified biological pump while CO_2 sequestration was supported by enhanced seawater alkalinity.

B4 Model limitations

Model parametrizations were chosen to the best of our knowledge. It should, however, be noted that key processes such as glacial changes in POC and P burial efficiency are only poorly constrained by available data. Moreover, we assumed that the global mean morphology of continental margins was retained over the glacial cycle and that the average global change in relative sea-level was equal to eustatic sea-level change. This approach neglects the glacial isostatic adjustment, i.e. the glacial subsidence of northern land masses loaded by large ice sheets, the uplift in flanking regions, and the numerous far-field effects (Daly, 1934; Milne and Mitrovica, 2008). It also neglects changes in margin morphology induced by the erosion and down-slope transport of shelf sediments during glacial sea-level low-stands (Hay, 1994) and the deglacial tilting of continental margins (Clark et al., 1978). Moreover, we assumed that during the LGM eustatic sea-level was 120 m lower than today while growing evidence supports the view that LGM sea-level fall was in fact larger than this consensus value (Austermann et al., 2013; Lambeck et al., 2014). The changes in the size of depositional and exposed areas at continental margins applied in the model should thus be regarded as rough estimates. Clearly, more work needs to be done to improve these estimates. However, there is no doubt that ocean margins retreated into steeper terrain while large shelf areas were exposed during glacial marine regressions and that these changes had a profound effect on glacial seawater composition and atmospheric pCO_2.

The accumulation of terrestrial POC in marine sediments was not considered in our model. Moreover, our model did not consider the growth of land plants and soil formation on emerged shelf regions during glacial sea-level low-stands. Trees and other plants may use sediment nutrients after shelf exposure and accumulate terrestrial POC on the emerged shelf. However, we think that the POC accumulation associated with these processes is small compared to the sedimentary POC turnover considered in the model. Modern continental margins (shelf and rise) accumulate sedimentary POC at a rate of about 100–200 $Gt\,kyr^{-1}$ (Hedges and Keil, 1995; Burdige, 2007; Wallmann et al., 2012; Dunne et al., 2007). This enormous flux is induced by the high marine productivity of the region and the rapid accumulation of sediments facilitating the burial of marine POC. Trees and soils growing on the emerged shelf would have to accumulate POC in the order of 10 000 Gt C to maintain this high carbon flux over the glacial period (ca. 80 kyr), an unlikely scenario since the global terrestrial carbon stock is ≤ 5000 GtC. The standing stock of POC in margin sediments exceeds the global terrestrial stock since POC is buried and preserved more efficiently in sediments than in most soils and plants. Sedimentary POC burial and preservation are promoted by high sedimentation rates and the lack of oxygen in these water-saturated deposits.

Appendix C: Model results

Key model results are listed in Tables C1 to C4 and compared to proxy data where available.

Table C1. Deep-sea CO_3^{2-} concentrations (in µmol kg^{-1}): differences between 21 and 5 ka calculated in the standard simulation STD are compared to corresponding observational data (derived from B / Ca ratios in foraminifera, LGM–Holocene differences).

Box	Model	Data	Sites/References
AR_D	36	24 ± 10	60° N, 24° W, 2.4 km (Yu et al., 2008)
NA_D	23	18 ± 9	55° N, 20° W, 2.0 km (Yu et al., 2008)
		24 ± 10	60° N, 24° W, 2.4 km (Yu et al., 2008)
		4 ± 6	55° N, 21° W, 2.8 km (Yu et al., 2008)
		-18 ± 8	51° N, 22° W, 3.5 km (Yu et al., 2008)
		-19 ± 9	52° N, 22° W, 4.0 km (Yu et al., 2008)
NA_B	15	-19 ± 9	52° N, 22° W, 4.0 km (Yu et al., 2008)
TA_D	14	9 ± 10	4° S, 13° W, 2.9 km (Raitzsch et al., 2011)
TA_B	6	-17 ± 12	4° S, 16° W, 4.7 km (Raitzsch et al., 2011)
SO_B	1	3 ± 2	41° S, 8° E, 5.0 km (Yu et al., 2014)
TIP_D	3	2 ± 3	0° S, 158° E, 2.3 km (Yu et al., 2010)
		-6 ± 4	0° S, 161° E, 3.4 km (Yu et al., 2010)
TIP_B	2	1 ± 4	1° S, 140° W, 4.3 km (Yu et al., 2013)
		5 ± 3	10° S, 52° E, 4.1 km (Yu et al., 2010)

Table C2. Effect of radiocarbon production rate on atmospheric and marine ^{14}C values under steady-state conditions. $R_{14}(0)$ is the pre-human atmospheric production rate applied in the model calibration (1.64 atoms cm^{-2} s^{-1} = 437 mol yr^{-1}).

Rate	$\Delta^{14}C$-CO_2 (‰)	$\Delta^{14}C$-DIC (‰)	$\Delta\Delta^{14}C$-DIC (‰)
$R_{14}(0)$	+0	−148	−148
$1.5 \times R_{14}(0)$	+500	+278	−222
$2.0 \times R_{14}(0)$	+1000	+704	−296

Table C3. $\Delta\Delta^{14}$C-DIC for the LGM (19–23 kyr BP) calculated in simulation STD and derived from radiocarbon measurements in foraminifera.

Box	Model	Data	Reference
AR_S	−196 to −177	EAST: −95 to −60	GIK 23074 (66°66.67′ N, 4°90′ E, 1157 m, Norw. Current),
		WEST: −210 to −240	Sarnthein et al. (2015) PS2644 (67°52.02′ N,
			21°45.92′ W, 777 m, East Greenland Current),
			Sarnthein et al. (2013, 2015)
AR_I	−206 to −187	−50	PS2644 (67°52.02′ N,
		−220 to −270	21°45.92′ W, 777 m), Sarnthein et al. (2013)
NA_S	−169 to −153	−115 to −40	MD90-917 (41°29.78′ N, 17°61.3′ E, 1010 m),
			MD99-2334K (37°48′ N, 10°10′ W, 3146 m),
			RAPID-17-5P (61°29′ N, 19°32′ W, 2303 m),
			Thornalley et al. (2011), MD08-3180 (38° N, 31°13.45′ W, 3064 m),
			Sarnthein et al. (2013)
NA_D	−257 to −228	−40 to −60	MD99-2334K (37°48′ N, 10°10′ W, 3146 m),
			RAPID-17-5P (61°29′ N, 19°32′ W, 2303 m),
			Thornalley et al. (2011)
		−260 to −275	MD08-3180 (38° N, 31°13.45′ W, 3064 m),
			Sarnthein et al. (2015)
NA_B	−285 to −253	−330	Extrapolated from Portuguese margin site
			MD99-2334K (37°48′ N, 10°10′ W, 3146 m),
			Skinner et al. (2014), assuming a transit time of ∼ 800 years
			from TNO57-21 (41°06′ S, 7°48′ E, 4981 m), Barker et al. (2010)
TA_S	−128 to −108	−130 to −95	ODP 1002 (10°42.37′ N, 65°10.18′ W, 893 m)
			and southward extrapolated from MD08-3180
			(38° N, 31°13.45′ W, 3064 m) Sarnthein et al. (2015)
TA_I	−241 to −218	−160 to −185 −85	Dredged coral transects at Gregg, Manning, and Muir Sea Mt. 33–39° N,
			< 2300 m, corr. according to Robinson et al. (2005)
SO_S	−160 to −140	−270 to −190	MD07-3076 (44°09′ S, 14°13′ W, 3770 m),
			Skinner et al. (2010)
SO_I	−228 to −201	−220 to −210	Dredged coral transect Drake Passage, < 1800 m,
			Burke et al. (1982) + AWI unpubl. data under review
SO_D	−332 to −296	−300 to −185	D07-3076 (44°09′ S, 14°13′ W, 3770 m),
			Atlantic sector, Skinner et al. (2010)
		−600 to −500	RV Sonne core transect off New Zealand, Pacific sector,
			AWI unpubl. records, under review
SO_B	−335 to −299	−230 to −130	TNO57-21 (41°06′ S, 7°48′ E, 4981 m),
			Barker et al. (2010)
TIP_S	−139 to −120	−220 to −105	MD01-2378 (13°08.25′ S, 121°78.8′ E, 1783 m),
			Sarnthein et al. (2015)
TIP_I	−238 to −211	−264 to −61	RC 27-14 (18.3° N, 57.6° E, 596 m)
		−205 to −190	RC 27-23 (18.0° N, 57.6° E, 820 m)
			Bryan et al. (2010)
		−220 to −165	MD01-2378 (13°08.25′ S, 121°78.8′ E, 1783 m),
			Sarnthein et al. (2013)
TIP_D	−363 to −324	−410 to −320	MD01-2378 (13°08.25′ S, 121°78.8′ E, 1783 m)
			GIK 17940 (20°07.0′ N, 117°23.0′ E, 1727 m)
			extrapolated to > 2000 m, Sarnthein et al. (2013)
NP_S	−156 to −137	−190 to −115	MD01-2416 (51°26.8′ N, 167°72.5′ E, 2317 m)
			MD02-2489 (54°39.07′ N, 148°92.13′ W, 3640 m)
			Sarnthein et al. (2013, 2015)
NP_D	−378 to −337	−470	MD01-2416 (51°26.8′ N, 167°72.5′ E, 2317 m)
			Sarnthein et al. (2013, 2015)
NP_B	−375 to −335	−270	MD02-2489 (54°39.07′ N, 148°92.13′ W, 3640 m)
			extrapolated to > 4000 m,
			Sarnthein et al. (2013), Gebhardt et al. (2008)

Table C4. LGM tracer concentrations in model boxes at 21 ka in simulation STD (see Tables A1 and A2 for further information).

Box	Sal (PSU)	PO_4 (µM)	NO_3 (µM)	O_2 (µM)	DIC (µM)	TA (µM)	$\delta^{13}C$ (‰)	$\Delta\Delta^{14}C$ (‰)
AR_S	33.69	0.93	12.2	369	2244	2562	1.63	−181
NA_S	35.84	0.34	4.2	266	2158	2619	2.56	−156
TA_S	36.94	0.14	1.7	214	2122	2685	2.90	−119
SO_S	35.80	0.42	6.0	306	2184	2588	2.38	−148
TIP_S	36.40	0.36	4.1	211	2040	2583	2.51	−128
NP_S	34.87	0.79	10.9	282	2131	2521	2.43	−145
AR_I	35.48	1.07	14.8	330	2268	2579	1.39	−192
NA_I	35.69	1.12	16.4	258	2277	2595	1.32	−192
TA_I	35.72	1.60	23.2	212	2345	2601	0.71	−224
SO_I	35.86	2.09	32.3	143	2419	2583	−0.13	−213
TIP_I	35.94	2.35	35.5	76	2444	2591	−0.38	−223
NP_I	35.72	2.97	42.1	69	2537	2631	−0.96	−300
AR_D	35.54	1.45	19.4	282	2315	2587	0.96	−221
NA_D	35.59	1.70	22.5	251	2346	2593	0.69	−239
TA_D	35.72	2.16	29.2	201	2422	2621	0.11	−281
SO_D	35.80	2.81	36.9	179	2518	2649	−0.60	−312
TIP_D	35.81	3.16	40.4	112	2576	2690	−0.83	−342
NP_D	35.79	3.12	40.6	108	2574	2691	−0.86	−356
AR_B	35.54	1.48	19.7	280	2317	2587	0.94	−222
NA_B	35.65	2.04	26.4	222	2392	2607	0.32	−266
TA_B	35.74	2.37	31.5	193	2453	2631	−0.11	−294
SO_B	35.80	2.84	37.1	174	2523	2654	−0.61	−315
TIP_B	35.81	3.06	39.0	135	2565	2694	−0.74	−334
NP_B	35.79	3.11	40.0	118	2574	2698	−0.81	−353

Appendix D: Radiocarbon model

A simple two-box model helps to explain why the ocean is strongly depleted in radiocarbon with respect to the atmosphere when radiocarbon production rates are high. In this model, radiocarbon is produced in the atmosphere and transferred from the atmosphere to the ocean by a diffusion-analogue process. It decays both in the atmosphere and in the ocean. At steady state, this simple system can be represented by the following set of equations:

atmosphere mass balance,

$$R_{14} - \lambda^{14}C_A - F_{AO} = 0; \quad \text{(D1)}$$

ocean mass balance,

$$F_{AO} - \lambda^{14}C_O = 0; \quad \text{(D2)}$$

and ^{14}C flux from atmosphere to ocean,

$$F_{AO} = k(^{14}C_A - ^{14}C_O), \quad \text{(D3)}$$

where R_{14} is the radiocarbon production rate, λ is the decay constant, $^{14}C_A$ is the radiocarbon mass in the atmosphere, $^{14}C_O$ is the radiocarbon mass in the ocean, and k is a mass transfer coefficient. Equations (D1)–(D3) can be combined and solved for the radiocarbon difference between atmosphere and ocean:

$$^{14}C_A - ^{14}C_O = \frac{R_{14}}{\lambda + 2 \cdot k}. \quad \text{(D4)}$$

The resulting equation shows that the difference is proportional to the radiocarbon production rate. The steady-state ^{14}C-depletion of the ocean with respect to the atmosphere, thus, increases under high production rates. The difference would vanish if the mass transport coefficient would be infinitely large. The example of the modern ocean shows, however, that this is not the case and that the ocean is significantly depleted in ^{14}C with respect to the atmosphere since the transfer of ^{14}C from the atmosphere into the ocean is too slow to eliminate the ^{14}C difference. In our simple two-box model, the radiocarbon flux is assumed to be proportional to the radiocarbon gradient between atmosphere and ocean (Eq. D3). The gradient increases under high production rates such that more ^{14}C is transferred from the ^{14}C-enriched atmosphere into the depleted ocean. The rate of radioactive decay in the ocean ($\lambda^{14}C_O$) increases since the ^{14}C content of the ocean is raised by the enhanced radiocarbon flux from the atmosphere. Steady state is attained when the decay rate in the ocean and the ^{14}C flux from the atmosphere are balanced (Eq. D2). The steady-state gradient ($^{14}C_A$–$^{14}C_O$), thus, increases in proportion to the atmospheric production rate such that the flux into the ocean compensates for the elevated decay rate in the ocean. The analytical solution for the simple two-box model (Eq. D4) correctly predicts the steady-state behaviour of our more evolved model system where the ocean is represented by 24 boxes and the radiocarbon uptake from the atmosphere is calculated applying Eq. (A12) rather than Eq. (D3). It predicts that $\Delta\Delta^{14}C$-DIC increases linearly with production rate as observed in the steady-state simulations (Table C2). The real ocean–atmosphere system is obviously more complex than any kind of model. However, the simple two-box model captures the basic features of the real system and reveals that the ^{14}C contrast increases in proportion to the production rate. Since radiocarbon production rates may have changed significantly over the last glacial cycle, this basic system property has to be considered in the interpretation of the marine ^{14}C-record.

Acknowledgements. This work was funded by the DFG via the collaborative project SFB 754. The paper was greatly improved in the review process thanks to the very helpful comments by the two reviewers (Victor Brovkin and anonymous) and the associated editor (Luke Skinner).

The article processing charges for this open-access publication were covered by a Research Centre of the Helmholtz Association.

Edited by: L. Skinner

References

Abe-Ouchi, A., Saito, F., Kawamura, K., Raymo, M. E., Okuno, J., Takahashi, K., and Blatter, H.: Insolation-driven 100 000-year glacial cycles and hysteresis of ice-sheet volume, Nature, 500, 190–193, doi:10.1038/nature12374, 2013.

Adkins, J. F. and Boyle, E. A.: Changing atmospheric $\Delta^{14}C$ and the record of deep water paleoventilation ages, Paleoceanography, 12, 337–344, 1997.

Altabet, M. A., Francois, R., Murray, D. W., and Prell, W. L.: Climate-related variations in denitrification in the Arabian Sea from sediment $^{15}N/^{14}N$ ratios, Nature, 373, 506–509, 1995.

Anderson, L. D., Delaney, M. L., and Faul, K. L.: Carbon to phosphorus ratios in sediments: Implications for nutrient cycling, Global Biogeochem. Cy., 15, 65–79, 2001.

Anderson, R. F., Ali, S., Bradtmiller, L. I., Nielsen, S. H. H., Fleisher, M. Q., Anderson, B. E., and Burckle, L. H.: Wind-driven upwelling in the Southern Ocean and the deglacial rise in atmospheric CO_2, Science, 323, 1443–1448, 2009.

Archer, D. E., Morford, J. L., and Emerson, S. R.: A model of suboxic sedimentary diagenesis suitable for automatic tuning and gridded global domains, Global Biogeochem. Cy., 16, 1017, doi:10.1029/2000GB001288, 2002.

Aumont, O. and Bopp, L.: Globalizing results from ocean in situ iron fertilization studies, Global Biogeochem. Cy., 20, GB2017, doi:10.1029/2005GB002591, 2006.

Austermann, J., Mitrovica, J. X., Latychev, K., and Milne, G. A.: Barbados-based estimate of ice volume at Last Glacial Maximum affected by subducted plate, Nat. Geosci., 6, 553–557, 2013.

Barker, S., Knorr, G., Vautravers, M. J., Diz, P., and Skinner, L. C.: Extreme deepening of the Atlantic overturning circulation during deglaciation, Nat. Geosci., 3, 567–571, 2010.

Baturin, G. N.: Issue of the relationship between primary productivity of organic carbon in ocean and phosphate accumulation (Holocene – Late Jurassic), Lithol. Miner. Resour., 42, 318–348, 2007.

Baturin, G. N. and Savenko, V. S.: Phosphorus in oceanic sedimentogenesis, Oceanology, 37, 107–113, 1997.

Berelson, W. E., Balch, W. M., Najjar, R., Feely, R. A., Sabine, C., and Lee, K.: Relating estimates of $CaCO_3$ production, export, and dissolution in the water column to measurements of $CaCO_3$ rain into sediment traps and dissolution on the sea floor: A revised global carbonate budget, Global Biogeochem. Cy., 21, GB1024, doi:10.1029/2006GB002803, 2007.

Berger, A. and Loutre, M. F.: Insolation values for the climate of the last 10 Million years, Quaternary Sci. Rev., 10, 297–317, 1991.

Berger, W. H.: Increase of carbon dioxide in the atmosphere during deglaciation: The coral reef hypothesis, Naturwissenschaften, 69, 87–88, 1982.

Berner, R. A.: Burial of organic carbon and pyrite sulfur in the modern ocean: Its geochemical and environmental significance, Am. J. Sci., 282, 451–473, 1982.

Berner, R. A.: The Phanerozoic Carbon Cycle: CO_2 and O_2, Oxford University Press, Oxford, 150 pp., 2004.

Berner, R. A. and Rao, J.-J.: Phosphorus in sediments of the Amazon River and estuary: Implications for the global flux of phosphorus to the sea, Geochim. Cosmochim. Ac., 58, 2333–2339, 1994.

Bohlen, L., Dale, A., and Wallmann, K.: Simple transfer functions for calculating benthic fixed nitrogen losses and C:N:P regeneration ratios in global biogeochemical models, Global Biogeochem. Cy., 26, GB3029, doi:10.1029/2011GB004198, 2012.

Bordelon-Katrynski, L. A. and Schneider, B.: Feedbacks of CO_2 dependent dissolved organic carbon production on atmospheric CO_2 in an ocean biogeochemical model, Biogeosciences Discuss., 9, 7983–8011, doi:10.5194/bgd-9-7983-2012, 2012.

Boyle, E. A. and Keigwin, L. D.: Deep circulation of the North Atlantic over the last 200 000 years: Geochemical evidence, Science, 218, 784–787, 1982.

Broecker, W. S.: Glacial to interglacial changes in ocean chemistry, Prog. Oceanogr., 11, 151–197, 1982a.

Broecker, W. S.: Ocean chemistry during glacial time, Geochim. Cosmochim. Ac., 46, 1689–1705, 1982b.

Broecker, W. S.: The great ocean conveyor, Oceanography, 4, 79–90, 1991.

Broecker, W. S., Peacock, S. L., Walker, S., Weiss, R., Fahrbach, E., Schroeder, M., Mikolajewic, U., Heinze, C., Key, R., Peng, T.-H., and Rubin, S.: How much deep water is formed in the Southern Ocean?, J. Geophys. Res., 103, 15833–15843, 1998.

Broecker, W. S., Clark, E., Hajdas, I., and Bonani, G.: Glacial ventilation rates for the deep Pacific Ocean, Paleoceanography, 19, PA2002, doi:10.1029/2003PA000974, 2004.

Brovkin, V. and Ganopolski, A.: The role of the terrestrial biosphere in CLIMBER-2 simulations of the last 4 glacial CO_2 cycles, Nova Acta Leopoldina NF, 121, 43–47, 2015.

Brovkin, V., Ganopolski, A., Archer, D., and Munhoven, G.: Glacial CO_2 cycle as a succession of key physical and biogeochemical processes, Clim. Past, 8, 251–264, doi:10.5194/cp-8-251-2012, 2012.

Bryan, S. P., Marchitto, T. M., and Lehman, S. J.: The release of ^{14}C-depleted carbon from the deep ocean during the last deglaciation: Evidence from the Arabian Sea, Earth Planet. Sci. Lett., 298, 244–254, 2010.

Burdige, D. J.: Preservation of organic matter in marine sediments: Controls, mechanisms, and an imbalance in sediment organic carbon budgets?, Chem. Rev., 107, 467–485, 2007.

Burke, W. H., Denison, R. E., Hetherington, E. A., Koepnick, R. B., Nelson, H. F., and Otto, J. B.: Variation of seawater $^{87}Sr/^{86}Sr$ throughout Phanerozoic time, Geology, 10, 516–519, 1982.

Burwicz, E. B., Rüpke, L. H., and Wallmann, K.: Estimation of the global amount of submarine gas hydrates formed via microbial methane formation based on numerical reaction-transport modeling and a novel parameterization of Holocene sedimentation, Geochim. Cosmochim. Acta, 75, 4562–4576, 2011.

Clark, J. A., Farrell, W. E., and Peltier, W. R.: Global changes in postglacial sea level: A numerical calculation, Quaternary Sci. Rev., 9, 265–287, 1978.

Conkright, M. E., Locarnini, R. A., Garcia, H. E., O'Brien, T. D., Boyer, T. P., Stephens, C., and Antonov, J. I.: World Ocean Atlas 2001: Objective Analyses, Data Statistics, and Figures, National Oceanographic Data Center, Silver Spring, MD, 17, 2002.

Curry, W. B. and Oppo, D. W.: Glacial water mass geometry and the distribution of $d^{13}C$ of SCO_2 in the western Atlantic Ocean, Paleoceanography, 20, PA1017, doi:10.1029/2004PA001021, 2005.

Dale, A. W., Sommer, S., Lomnitz, U., Montes, I., Treude, T., Liebetrau, V., Gier, J., Hensen, C., Dengler, M., Stolpovsky, K., Bryant, L. D., and Wallmann, K.: Organic carbon production, mineralisation and preservation on the Peruvian margin, Biogeosciences, 12, 1537–1559, doi:10.5194/bg-12-1537-2015, 2015.

Daly, R. A.: The Changing World of the Ice Age, Yale University Press, New Haven, 1934.

Denton, G. H., Anderson, R. F., Toggweiler, J. R., Edwards, R. L., Schaefer, J. M., and Putnam, A. E.: The Last Glacial Termination, Science, 328, 1652–1656, 2010.

Deutsch, C., Gruber, N., Key, R. M., and Sarmiento, J. L.: Denitrification and N_2 fixation in the Pacific Ocean, Global Biogeochem. Cy., 15, 483–506, 2001.

Deutsch, C., Sigman, D. M., Thunell, R. C., Meckler, A. N., and Haug, G. H.: Isotopic constraints on glacial/interglacial changes in the oceanic nitrogen budget, Global Biogeochem. Cy., 18, GB4012, doi:10.1029/2003GB002189, 2004.

Dunne, J. P., Sarmiento, J. L., and Gnanadesikan, A.: A synthesis of global particle export from the surface ocean and cycling through the ocean interior and on the seafloor, Global Biogeochem. Cy., 21, GB4006, doi:10.1029/2006GB002907, 2007.

Duplessy, J. C., Shackleton, N. J., Fairbanks, R. G., Labeyrie, L., Oppo, D., and Kallel, N.: Deepwater source variations during the last climatic cycle and their impact on the global deepwater circulation, Paleoceanography, 3, 343–360, 1988.

Eakins, B. W. and Sharman, G. F.: Hypsographic curve of Earth's surface from ETOPO1, NOAA National Geophysical Data Center, Boulder, CO, 2012.

Eugster, O., Gruber, N., Deutsch, C., Jaccard, S. L., and Payne, M. R.: The dynamics of the marine nitrogen cycle across the last deglaciation, Paleoceanography, 28, 116–129, doi:10.1002/palo.20020, 2013.

Frank, M., Schwarz, B., Baumann, S., Kubik, P. W., Suter, M., and Mangini, A.: A 200 kyr record of cosmogenic radionuclide production rate and geomagnetic field intensity from ^{10}Be in globally stacked deep-sea sediments, Earth Planet. Sci. Lett., 149, 121–129, 1997.

Franke, J., Paul, A., and Schulz, M.: Modeling variations of marine reservoir ages during the last 45 000 years, Clim. Past, 4, 125–136, doi:10.5194/cp-4-125-2008, 2008.

Froelich, P. N., Bender, M. L., Luedtke, N. A., Heath, G. R., and DeVries, T.: The marine phosphorus cycle, Am. J. Sci., 282, 474–511, 1982.

Ganopolski, A. and Calov, R.: The role of orbital forcing, carbon dioxide and regolith in 100 kyr glacial cycles, Clim. Past, 7, 1415–1425, doi:10.5194/cp-7-1415-2011, 2011.

Ganopolski, A., Rahmstorf, S., Petoukhov, V., and Claussen, M.: Simulation of modern and glacial climates with a coupled global model of intermediate complexity, Nature, 391, 351–356, 1998.

Ganopolski, A., Calov, R., and Claussen, M.: Simulation of the last glacial cycle with a coupled climate ice-sheet model of intermediate complexity, Clim. Past, 6, 229–244, doi:10.5194/cp-6-229-2010, 2010.

García, H. E. and Gordon, L. I.: Oxygen solubility in seawater: Better fitting equations, Limnol. Oceanogr., 37, 1307–1312, 1992.

Gebhardt, H., Sarnthein, M., Grootes, P. M., Kiefer, T., Kuehn, H., Schmieder, F., and Röhl, U.: Paleonutrient and productivity records from the subarctic North Pacific for Pleistocene glacial terminations I to V, Paleoceanography, 23, PA4212, doi:10.1029/2007PA001513, 2008.

Gehlen, M., Bopp, L., Emprin, N., Aumont, O., Heinze, C., and Ragueneau, O.: Reconciling surface ocean productivity, export fluxes and sediment composition in a global biogeochemical ocean model, Biogeosciences, 3, 521–537, doi:10.5194/bg-3-521-2006, 2006.

Gnanadesekian, A. and Hallberg, R.: Physical oceanography, thermal structure and general circulation, in: Encyclopedia of Physical Science and Technology, edited by: Meyers, R. A., Academic Press, San Diego, 189–210, 2002.

Hartnett, H. E., Keil, R. G., Hedges, J. I., and Devol, A. H.: Influence of oxygen exposure time on organic carbon preservation in continental margin sediments, Nature, 391, 572–574, 1998.

Hay, W. W.: Pleistocene-Holocene Fluxes Are Not the Earth's Norm, in: Material Fluxes on the Surface of the Earth, edited by: Hay, W. W. and Usselman, T., Studies in Geophysics, National Academy Press, Washington, 15–27, 1994.

Hay, W. W. and Southam, J. R.: Modulation of marine sedimentation by the continental shelves, in: The Fate of Fossil Fuel CO_2 in the Oceans, edited by: Andersen, N. R. and Malahoff, A., Plenum Press, New York, 569–604, 1977.

Hedges, J. I. and Keil, R. G.: Sedimentary organic matter preservation: an assessment and speculative synthesis, Mar. Chem., 49, 81–115, 1995.

Heinze, C., Maier-Reimer, E., Winguth, A. M. E., and Archer, D.: A global oceanic sediment model for long-term climate studies, Global Biogeochem. Cy., 13, 221–250, 1999.

Honjo, S., Manganini, S. J., Krishfield, R. A., and Francois, R.: Particulate organic carbon fluxes to the ocean interior and factors controlling the biological pump: A synthesis of global sediment trap programs since 1983, Progr. Oceanogr., 76, 217–285, doi:10.1016/j.pocean.2007.11.003, 2008.

Imbrie, J. and Imbrie, J. Z.: Modeling the climatic response to orbital variations, Science, 207, 943–953, 1980.

Imbrie, J., Berger, A., E. A., B., Clemens, S. C., Duffy, A., Howard, W. R., Kukja, G., Kutzbach, J., Martinson, D. G., McIntyre, A., Mix, A. C., Molfino, B., Morley, J. J., Peterson, L. C., Pjsias, N. G., Prell, W. L., Raymo, M. E., Shackleton, N. J., and Toggweiler, J. R.: On the structure and origin of major glaciation cycles 2, The 100 000-year cycle, Paleoceanography, 8, 699–735, 1993.

Ingall, E. D. and Jahnke, R. A.: Evidence for enhanced phosphorus regeneration from marine sediments overlain by oxygen depleted waters, Geochim. Cosmochim. Ac., 58, 2571–2575, 1994.

Jaccard, S. L. and Galbraith, E. D.: Large climate-driven changes of oceanic oxygen concentrations during the last deglaciation, Nat. Geosci., 5, 151–156, 2012.

Jahnke, R. A.: The global ocean flux of particulate organic carbon: Areal distribution and magnitude, Global Biogeochem. Cy., 10, 71–88, 1996.

Key, R. M., Kozyr, A., Sabine, C. L., Lee, K., Wanninkhof, R., Bullister, J. L., Feely, R. A., Millero, F. J., Mordy, C., and Peng, T.-H.: A global ocean carbon climatology: Results from Global Data Analysis Project (GLODAP), Global Biogeochem. Cy., 18, GB4031, doi:10.1029/2004GB002247, 2004.

Kleypas, J. A.: Modeled estimates of global reef habitat and carbonate production since the last glacial maximum, Paleoceanogr., 12, 533–545, 1997.

Köhler, P. and Fischer, H.: Simulating changes in the terrestrial biosphere during the last glacial/interglacial transition, Global Planet. Change, 43, 33–55, 2004.

Köhler, P., Fischer, H., Munhoven, G., and Zeebe, R. E.: Quantitative interpretation of atmospheric carbon records over the last glacial termination, Global Biogeochem. Cy., 19, GB4020, doi:10.1029/2004GB002345, 2005.

Köhler, P., Muscheler, R., and Schmitt, J.: A model-based interpretation of low-frequency changes in the carbon cycle during the last 120 000 years and its implications for the reconstruction of atmospheric $\Delta^{14}C$, Geochem. Geophys. Geosys., 7, Q11N06, doi:10.1029/2008PA001703, 2006.

Körtzinger, A., Hedges, J. I., and Quay, P. D.: Redfield ratios revisited: Removing the biasing effect of anthropogenic CO_2, Limnol. Oceanogr., 46, 964–970, 2001.

Krom, M. D. and Berner, R. A.: The diagenesis of phosphorus in a nearshore marine sediment, Geochim. Cosmochim. Ac., 45, 207–216, 1981.

Laj, C., Kissel, C., Mazaud, A., Michel, E., Muscheler, R., and Beer, J.: Geomagnetic field intensity, North Atlantic Deep Water circulation and atmospheric $D^{14}C$ during the last 50 kyr, Earth Planet. Sci. Lett., 200, 177–190, 2002.

Lambeck, K., Rouby, H., Purcell, A., Sun, Y., and Sambridge, M.: Sea level and global ice volumes from the Last Glacial Maximum to the Holocene, P. Natl. Acad. Sci. USA, 111, 15296–15303, 2014.

Lambert, F., Tagliabue, A., Shaffer, G., Lamy, F., Winckler, G., Farias, L., Gallardo, L., and De Pol-Holz, R.: Dust fluxes and iron fertilization in Holocene and Last Glacial Maximum climates, Geophys. Res. Lett., 42, 6014–6023, doi:10.1002/2015gl064250, 2015.

Lomnitz, U., Sommer, S., Dale, A. W., Löscher, C. R., ke, A. N., K. Wallmann, and Hensen, C.: Benthic phosphorus cycling in the Peruvian oxygen minimum zone, Biogeosciences Discuss., 12, 16755–16801, doi:10.5194/bgd-12-16755-2015, 2015.

Madec, G., Delecluse, P., Imbard, M., and Levy, C.: OPA8.1 Ocean general circulation model reference manual, Notes du pôle de modél. 11, Inst. Pierre-Simon Laplace, Paris, 91, 1998.

Marcott, S. A., Bauska, T. K., Buizert, C., Steig, E. J., Rosen, J. L., Cuffey, K. M., Fudge, T. J., Severinghaus, J. P., Ahn, J., Kalk, M. L., McConnell, J. R., Sowers, T., Taylor, K. C., White, J. W. C., and Brook, E. J.: Centennial-scale changes in the global carbon cycle during the last deglaciation, Nature, 514, 616–619, 2014.

Marinov, I., Gnanadesikan, A., Toggweiler, J. R., and Sarmiento, J. L.: The Southern Ocean biogechemcial divide, Nature, 441, 964–967, 2006.

Martin, J. H.: Glacial-interglacial CO_2 change: The iron hypothesis, Paleoceanography, 5, 1–13, 1990.

Martınez-Garcia, A., Sigman, D. M., Ren, H., Anderson, R. F., Straub, M., Hodell, D. A., Jaccard, S. L., Eglinton, T., and Haug, G. H.: Iron fertilization of the Subantarctic Ocean during the last ice age, Science, 343, 1347–1350, 2014.

Mayer, L. M., Schick, L. L., Hardy, K. R., Wagal, R., and McCarthy, J.: Organic matter in small mesopores in sediments and soils, Geochim. Cosmochim. Ac., 68, 3863–3872, 2004.

McManus, J. F., Francois, R., Gherardi, J.-M., Keigwin, L. D., and Brown-Leger, S.: Collapse and rapid resumption of Atlantic meridional circulation linked to deglacial climate changes, Nature, 428, 834–837, 2004.

Menviel, L., Joos, F., and Ritz, S. P.: Simulating atmospheric CO_2, C-13 and the marine carbon cycle during the Last Glacial-Interglacial cycle: possible role for a deepening of the mean remineralization depth and an increase in the oceanic nutrient inventory, Quaternary Sci. Rev., 56, 46–68, doi:10.1016/j.quascirev.2012.09.012, 2012.

Middelburg, J. J., Soetaert, K., Herman, P. M. J., and Heip, C. H. R.: Denitrification in marine sediments: A model study, Global Biogeochem. Cy., 10, 661–673, 1996.

Milankovitch, M.: Kanon der Erdbestrahlung und Seine Anwendung auf das Eiszeitenproblem, Royal Serbian Academy Special Publication, Royal Serbian Academy, Belgrade, Serbia, 1941.

Milliman, J. D. and Droxler, A. W.: Neritic and pelagic carbonate sedimentation in the marine environment: ignorance is not a bliss, Geol. Rundsch., 85, 496–504, 1996.

Milne, G. A. and Mitrovica, J. X.: Searching for eustasy in deglacial sea-level histories, Quaternary Sci. Rev., 27, 2292–2302, 2008.

Monnin, E., Indermühle, A., Dallenbach, A., Flückiger, J., Stauffer, B., Stocker, T. F., Raynaud, D., and Barnola, J.-M.: Atmospheric CO_2 concentrations over the Last Glacial Termination, Science, 291, 112–114, 2001.

Monnin, E., Steig, E. J., Siegenthaler, U., Kawamura, K., Schwander, J., Stauffer, B., Stocker, T. F., Morse, D. L., Barnola, J.-M., Bellier, B., Raynaud, D., and Fischer, H.: Evidence for substantial accumulation rate variability in Antarctica during the Holocene, through synchronization of CO_2 in the Taylor Dome, Dome C and DML ice cores, Earth Planet. Sci. Lett., 224, 45–54, 2004.

Mook, W. G. and Plicht, J. v. d.: Reporting C-14 activities and concentrations, Radiocarbon, 41, 227–239, 1999.

Munhoven, G.: Glacial-interglacial changes of continental weathering: estimates of the related CO_2 and HCO_3^- flux variations and their uncertainties, Global Planet. Change, 33, 155–176, 2002.

Muscheler, R., Beer, J., Kubik, P. W., and Synal, H.-A.: Geomagnetic field intensity during the last 60,000 years based on ^{10}Be and ^{36}Cl from the Summit ice cores and ^{14}C., Quaternary Sci. Rev., 24, 1849–1860, 2005.

Noffke, A., Hensen, C., Sommer, S., Scholz, F., Bohlen, L., Mosch, T., Graco, M., and Wallmann, K.: Benthic iron and phosphorus fluxes across the Peruvian oxygen minimum zone, Limnol. Oceanogr., 57, 851–867, 2012.

Oliver, K. I. C., Hoogakker, B. A. A., Crowhurst, S., Henderson, G. M., Rickaby, R. E. M., Edwards, N. R., and Elderfield, H.: A synthesis of marine sediment core $\delta^{13}C$ data over the last 150 000 years, Clim. Past, 6, 645–673, doi:10.5194/cp-6-645-2010, 2010.

Opdyke, B. N. and Walker, J. C. G.: Return of the coral reef hypothesis: Basin to shelf partitioning of $CaCO_3$ and its effect on atmospheric CO_2, Geology, 20, 733–736, 1992.

Peterson, C. D., Lisiecki, L. E., and Stern, J. V.: Deglacial whole-ocean δ13C change estimated from 480 benthic foraminiferal records, Paleoceanography, 29, 549–563, doi:10.1002/2013PA002552, 2014.

Petit, L. R., Jouzel, J., Raynaud, D., Barkov, N. I., Barnola, J.-M., Basile, I., Bender, M., Chappelaz, J., Davis, M., Delaygue, G., Delmotte, M., Kotlyakov, V. M., Legrand, M., Lipenkov, V. Y., Lorius, C., Pépin, L., Ritz, C., Saltzman, E., and Stievenard, M.: Climate and atmospheric history of the past 420 000 years from the Vostok ice core, Antarctica, Nature, 399, 429–436, 1999.

Piotrowski, A. M., Goldstein, S. L., Hemming, S. R., and Fairbanks, R. G.: Temporal relationships of carbon cycling and ocean circulation at glacial boundaries, Science, 307, 1933–1937, 2005.

Pollard, D.: Ice-age simulations with a calving ice-sheet model, Quaternary Research, 20, 30–48, 1983.

Rae, J. W. B., Sarnthein, M., Foster, G. L., Ridgwell, A., Grootes, P. M., and Elliott., T.: Deep water formation in the North Pacific and deglacial CO_2 rise, Paleoceanography, 29, 645–667, doi:10.1002/2013PA002570, 2014.

Raitzsch, M., Hathorne, E. C., Kuhnert, H., Groeneveld, J., and Bickert, T.: Modern and late Pleistocene B / Ca ratios of the benthic foraminifer *Planulina wuellerstorfi* determined with laser ablation ICP-MS, Geology, 39, 1039–1042, 2011.

Raymo, M. E., Oppo, D. W., and Curry, W.: The mid-Pleistocene climate transition: A deep sea carbon isotope perspective, Paleoceanogr., 12, 546–559, 1997.

Redfield, A. C.: The biological control of chemical factors in the environment, American Scientist, 46, 205–221, 1958.

Reimer, P. J., Bard, E., Bayliss, A., Beck, J. W., Blackwell, P. G., Ramsey, C. B., Buck, C. E., Cheng, H., Edwards, R. L., Friedrich, M., Grootes, P. M., Guilderson, T. P., Haflidason, H., Hajdas, I., Hatté, C., Heaton, T. J., Hoffmann, D. L., Hogg, A. G., Hughen, K. A., Kaiser, K. F., Kromer, B., Manning, S. W., Niu, M., Reimer, R. W., Richards, D. A., Scott, E. M., Southon, J. R., Staff, R. A., Turney, C. S. M., and Plicht, J. v. D.: IntCal13 and marine13 radiocarbon age calibration curves 0–50 000 years Cal BP, Radiocarbon, 55, 1869–1887, 2013.

Ridgewell, A.: Glacial-interglacial perturbations in the global carbon cycle, PhD, University of East Anglia, Norwich, UK, 2001.

Roberts, N. L., Piotrowski, A. M., McManus, J. F., and Keigwin, L. D.: Synchronous deglacial overturning and water mass source changes, Science, 327, 75–78, 2010.

Robinson, L. F., Adkins, J. F., Keigwin, L. D., Southon, J., Fernandez, D. P., Wang, S.-L., and Scheirer, D. S.: Radiocarbon Variability in the Western North Atlantic During the Last Deglaciation, Science, 310, 1469–1473, 2005.

Romanek, C. S., Grossman, E. L., and Morse, J. W.: Carbon isotope fractionation in synthetic aragonite and calcite: Effects of temperature and precipitation rate, Geochim. Cosmochim. Ac., 56, 419–430, 1992.

Roth, R., Ritz, S. P., and Joos, F.: Burial-nutrient feedbacks amplify the sensitivity of atmospheric carbon dioxide to changes in organic matter remineralisation, Earth Syst. Dynam., 5, 321–343, doi:10.5194/esd-5-321-2014, 2014.

Ruddiman, W. F., Fuller, D. Q., Kutzbach, J. E., Tzedakis, P. C., Kaplan, J. O., Ellis, E. C., Vavrus, S. J., Roberts, C. N., Fyfe, R., He, F., Lemmen, C., and Woodbridge, J.: Late Holocene climate: natural or anthropogenic, Rev. Geophys., online first, doi:10.1002/2015RG000503, 2016.

Ruttenberg, K. C.: Development of a sequential extraction method for different forms of phosphorus in marine sediments, Limnol. Oceanogr., 37, 1460–1482, 1992.

Ruttenberg, K. C. and Berner, R. A.: Authigenic apatite formation and burial in sediments from non-upwelling, continental margin environments, Geochim. Cosmochim. Ac., 57, 991–1007, 1993.

Sarmiento, J. L. and Gruber, N.: Ocean Biogeochemical Cycles, Princeton University Press, Princeton, 503 pp., 2006.

Sarnthein, M., Winn, K., Jung, S. J. A., Duplessy, J.-C., Labeyrie, L., Erlenkeuser, H., and Ganssen, G.: Changes in east Atlantic deepwater circulation over the last 30 000 years: Eight time slice reconstructions, Paleoceanography, 9, 209–267, 1994.

Sarnthein, M., Schneider, B., and Grootes, P. M.: Peak glacial ^{14}C ventilation ages suggest major draw-down of carbon into the abyssal ocean, Clim. Past, 9, 2595–2614, doi:10.5194/cp-9-2595-2013, 2013.

Sarnthein, M., Balmer, S., Grootes, P. M., and Mudelsee, M.: Planktic and benthic ^{14}C reservoir ages for three ocean basins, calibrated by a suite of ^{14}C plateaus in the glacial-to-deglacial Suigetsu atmospheric ^{14}C record, Radiocarbon, 57, 129–151, 2015.

Schenau, S. J. and De Lange, G. J.: Phosphorus regeneration vs. burial in sediments of the Arabian Sea, Mar. Chem., 75, 201–217, 2001.

Schlünz, B., Schneider, R. R., Müller, P. J., Swowers, W. J., and Wefer, G.: Terrestrial organic carbon accumulation on the Amazon deep sea fan during the last glacial sea level stand, Chem. Geol., 159, 263–281, 1999.

Schmitt, J., Schneider, R., Elsig, J., Leuenberger, D., Lourantou, A., Chappellaz, J., Köhler, P., Joos, F., Stocker, T. F., Leuenberger, M., and Fischer, H.: Carbon isotope constraints on the deglacial CO_2 rise from ice cores, Science, 336, 711–714, 2012.

Schmittner, A., Urban, N. M., Shakun, J. D., Mahowald, N. M., Clark, P. U., Bartlein, P. J., Mix, A. C., and Rosell-Melé, A.: Climate sensitivity estimated from temperature reconstructions of the Last Glacial Maximum, Science, 334, 1385–1388, 2011.

Schmittner, A., Gruber, N., Mix, A. C., Key, R. M., Tagliabue, A., and Westberry, T. K.: Biology and air-sea gas exchange controls on the distribution of carbon isotope ratios ($\delta^{13}C$) in the ocean, Biogeosciences, 10, 5793–5816, doi:10.5194/bg-10-5793-2013, 2013.

Seiter, K., Hensen, C., and Zabel, M.: Benthic carbon mineralization on a global scale, Global Biogeochem. Cy., 19, GB1010, doi:10.1029/2004GB002225, 2005.

Shackleton, N. J.: Carbon-13 in Uvigerina: Tropical rainforest history in the equatorial Pacific carbonate dissolution cycles, in: The Fate of Fossil Fuel in the Oceans, edited by: Andersen, N. R., and Malahoff, A., Plenum, New York, 401–427, 1977.

Skinner, L. C.: Glacial-interglacial atmospheric CO_2 change: a possible "standing volume" effect on deep-ocean carbon sequestration, Clim. Past, 5, 537–550, doi:10.5194/cp-5-537-2009, 2009.

Skinner, L. C., Fallon, S., Waelbroeck, C., Michel, E., and Barker, S.: Ventilation of the deep Southern Ocean and deglacial CO_2 rise, Science, 328, 1147–1151, 2010.

Skinner, L. C., Waelbroeck, C., Scrivner, A. E., and Fallon, S. J.: Radiocarbon evidence for alternating northern and southern sources of ventilation of the deep Atlantic carbon pool during the last deglaciation, P. Natl. Acad. Sci. USA, 111, 5480–5484, 2014.

Stanford, J. D., Hemingway, R., Rohling, E. J., Challenor, P. G., Medina-Elizalde, M., and Lester, A. J.: Sea-level probability for the last deglaciation: A statistical analysis of far-field records, Global Planet. Change, 79, 193–203, 2011.

Stolpovsky, K., Dale, A. W., and Wallmann, K.: Toward a parameterization of global-scale organic carbon mineralization kinetics in surface marine sediments, Global Biogeochem. Cy., 29, 812–829, doi:10.1002/2015gb005087, 2015.

Stuiver, M. and Polach, H. A.: Discussion: Reporting of ^{14}C data, Radiocarbon, 19, 355–363, 1977.

Suess, E.: Particulate organic carbon flux in the oceans – Surface productivity and oxygen utilization, Nature, 288, 260–263, 1980.

Tamburini, F. and Föllmi, K. B.: Phosphorus burial in the ocean over glacial-interglacial time scales, Biogeosciences, 6, 501–513, doi:10.5194/bg-6-501-2009, 2009.

Thornalley, D. J. R., Barker, S., Broecker, W. S., Elderfield, H., and McCave, N.: The Deglacial Evolution of North Atlantic Deep Convection, Science, 331, 202–205, 2011.

Toggweiler, J. R.: Variation of atmospheric CO_2 by ventilation of the ocean's deepest water, Paleoceanography, 14, 571–588, 1999.

Tschumi, T., Joos, F., Gehlen, M., and Heinze, C.: Deep ocean ventilation, carbon isotopes, marine sedimentation and the deglacial CO_2 rise, Clim. Past, 7, 771–800, doi:10.5194/cp-7-771-2011, 2011.

Tyrrell, T.: The relative influences of nitrogen and phosphorus on oceanic primary production, Nature, 400, 525–531, 1999.

Ushie, H. and Matsumoto, K.: The role of shelf nutrients on glacial-interglacial CO_2: A negative feedback, Global Biogeochem. Cy., 26, GB2039, doi:10.1029/2011GB004147, 2012.

Van Cappellen, P. and Ingall, E. D.: Benthic phosphorus regeneration, net primary production, and ocean anoxia: A model of the coupled marine biogeochemical cycles of carbon and phosphorus, Paleoceanography, 9, 677–692, 1994.

Waelbroeck, C., Labeyrie, L., Michel, E., Duplessy, J.-C., McManus, J. F., Lambeck, K., Balbon, E., and Labracherie, M.: Sea-level and deep water temperature changes derived from benthic foraminifera isotopic records, Quaternary Sci. Rev., 21, 295–305, 2002.

Wallmann, K.: Feedbacks between oceanic redox states and marine productivity: A model perspective focused on benthic phosphorus cycling, Global Biogeochem. Cy., 17, 1084, doi:10.1029GB001968, 2003.

Wallmann, K.: Phosphorus imbalance in the global ocean?, Global Biogeochem. Cy., 24, GB4030, doi:10.1029/2009GB003643, 2010.

Wallmann, K.: Is late Quaternary climate change governed by self-sustained oscillations in atmospheric CO_2?, Geochim. Cosmochim. Ac., 132, 413–439, 10.1016/j.gca.2013.10.046, 2014.

Wallmann, K., Pinero, E., Burwicz, E., Haeckel, M., Hensen, C., Dale, A., and Ruepke, L.: The global inventory of methane hydrate in marine sediments: A theoretical approach, Energies, 5, 2449–2498, 2012.

Walsh, J. J., Rowe, G. T., Iverson, R. L., and McRoy, C. P.: Biological export of shelf carbon is a sink of the global CO_2 cycle, Nature, 291, 196–201, 1981.

Watson, A. J., Vallis, G. K., and Nikurashin, M.: Southern Ocean buoyancy forcing of ocean ventilation and glacial atmospheric CO_2, Nat. Geosci., 8, 861–864, doi:10.1038/NGEO2538, 2015.

Yu, J., Elderfield, H., and Piotrowski, A. M.: Seawater carbonate ion-δ13C systematics and application to glacial-interglacial North Atlantic ocean circulation, Earth Planet. Sci. Lett., 271, 209–220, 2008.

Yu, J., Broecker, W. S., Elderfield, H., Jin, Z., McManus, J., and Zhang, F.: Loss of carbon from the deep sea since the Last Glacial Maximum, Science, 330, 1084–1087, 2010.

Yu, J., Anderson, R. F., Jin, Z., Rae, J. W. B., Opdyke, B. N., and Eggins, S. M.: Responses of the deep ocean carbonate system to carbon reorganization during the Last Glacial-interglacial cycle, Quaternary Sci. Rev., 76, 39–52, 2013.

Yu, J., Anderson, R. F., Jin, Z., Menviel, L., Zhang, F., Ryerson, F. J., and Rohling, E. J.: Deep South Atlantic carbonate chemistry and increased interocean deep water exchange during last deglaciation, Quaternary Sci. Rev., 90, 80–89, 2014.

Zeebe, R. and Wolf-Gladrow, D.: CO_2 in Seawater: Equilibrium, Kinetics and Isotopes, Elsevier Oceanography Series, Elsevier, Amsterdam, 346 pp., 2001.

Zhang, J., Quay, P. D., and Wilbur, D. O.: Carbon-isotope fractionation during gas-water exchange and dissolution of CO_2, Geochim. Cosmochim. Ac., 59, 107–114, 1995.